Development and analysis of high-order vorticity confinement schemes

I. Petropoulos [a,b,*], M. Costes [a], P. Cinnella [b]

[a] ONERA, The French Aerospace Lab, 8 rue des Vertugadins, F-92190 Meudon, France
[b] DynFluid Lab., Arts et Métiers ParisTech, 151 Boulevard de l'Hôpital, F-75013 Paris, France

Keywords:
Vorticity confinement
High-order schemes
Scalar transport equation
Spectral analysis
Euler/Navier–Stokes equations
High-order VC2 confinement scheme

A B S T R A C T

High-order extensions of the Vorticity Confinement (VC) method are developed for the accurate computation of vortical flows, following the VC2 conservative formulation of Steinhoff. First, a high-order formulation of VC is presented for the case of the linear transport equation for decoupled schemes in space and time. A spectral analysis shows that the new nonlinear schemes have improved dispersive and dissipative properties compared to their linear counterparts at all orders of accuracy. For the Euler and Navier–Stokes equations, the original VC method is extended to 3rd- and 5th-order of accuracy, with the goal of developing a VC formulation that maintains the vorticity preserving capability of the original 1st-order method and is suitable for application to high-order numerical simulations. The high-order extensions remain both independent of the choice of baseline numerical scheme and rotationally invariant since they are based on the Laplace operator. Numerical tests validate the increased order of accuracy, vorticity-preserving capability and compatibility of the VC extensions with high-order methods.

1. Introduction

Standard CFD methods have followed a course of steady improvement over the past decades and are adequate for modeling a large number of applications, but the accurate computation of vortical flows remains a challenge. The numerical schemes used in the solution of the flow equations need to be dissipative to ensure stability thus resulting in fast spreading and diffusion of vortex structures in computations. This weakness concerns both research and industry as the accurate advection of vortices is important in a broad spectrum of computational fluid dynamics applications such as wakes, vortex-structure interaction, separated flows and turbulence.

Lagrangian methods allow for a perfect preservation of vortices, but are usually inviscid and incompressible [1–3]. Also, they often require special treatment for different applications and can have difficulties in computing complex flow states (e.g. vortex merging). Such characteristics are hindering for the industry so these methods are rarely applied out of research for advanced aeronautics computations.

The formulation of Eulerian methods on the other hand is more robust and for this reason they are widely adopted. To treat the problem of vortex dissipation, the majority of the CFD community usually resorts to the use of finer meshes or automatic mesh adaptation methods [4–6] to increase the number of cells in the vicinity of vortical regions. However, there are drawbacks such as the significant increase of complexity and computational cost. Alternative hybrid methods to minimize the dissipation of vorticity can be constructed through domain decomposition by the coupling of structured-unstructured Eulerian [7,8] or Eulerian–Lagrangian solvers [9,10]. Such methods can combine the benefits of the different approaches in each region but are not always straightforward.

Another possibility is the use of high-order methods in the discretization of the fluid dynamics equations [11–13], which results in improved wave propagation properties. In the well-established Finite Volume method, the implementation of high-order flux derivatives is not simple, especially for non-Cartesian grids. Additionally, even using high-order methods, the dissipation of vortices cannot be corrected completely. Another possibility is to construct numerical schemes that ensure vorticity preservation at the discrete level [14,15]. However, this involves significant modifications of the existing solvers. Thus, a more general and less intrusive method for vorticity preservation remains interesting.

Such an alternative is the Vorticity Confinement (VC) method proposed by J. Steinhoff [16–18], designed to capture small-scale features directly on the computational grid. In the present work, we are working with the second (VC2) formulation [19,20] of the method to ensure discrete momentum conservation. The capability

* Corresponding author.
E-mail addresses: ilias.petropoulos@onera.fr (I. Petropoulos), mcostes@onera.fr (M. Costes), paola.cinnella@ensam.eu (P. Cinnella).

of VC to preserve vorticity has been verified by extensive application in the aeronautics field over the past two decades. However, the original method remains 1st-order accurate and vortex structures are rapidly dominated by the VC source term. This effect is more important when a higher-order baseline scheme is used, where the lower-order term deteriorates the overall accuracy in vortical flow regions.

Due to the growth of high-order methods in both research and industrial applications [21], the construction of a Vorticity Confinement method that is appropriate for high-order computations shows great interest. Even more so, since in the vast majority of cases VC can be applied independently of the choice of the underlying numerical scheme and is not restricted to a specific formulation. High-order extensions of VC were analyzed for the linear advection equation [22], showing that the asymptotic solution over long distances is the same for all orders of accuracy, albeit at a lower convergence rate for higher orders. The slower convergence rate is in accordance with the lower numerical error that is associated with higher-order schemes, indicating a sound basis for an extension to the Euler/Navier–Stokes equations. First results on the Euler equations were presented for helicopter applications [23] while the complete method and its consistency with high-order flux discretizations have been thoroughly validated [24].

In the present work, a scalar VC formulation is first presented for a family of schemes that are decoupled in space and time. This allows a more straightforward analysis of the numerical error associated with the space discretization compared to previous works, in which VC was based on high-order extensions of the Lax–Wendroff and Beam-Warming schemes. A spectral analysis of these schemes is then presented, comparing linear theory with a quasi-linear numerical method. Afterwards, the high-order VC extension methodology proposed in [24] is analyzed, demonstrating the analogy of these schemes with the scalar case and their equivalence with a nonlinear anti-diffusive flux correction applied in vortical flow regions. The high-order VC schemes are then evaluated through application in numerical simulations up to 5th-order of accuracy.

The article consists of the following parts. Section 2 explains the VC formulation and the higher-order extension methodology for the scalar advection case and the Euler/RANS equations. Section 3 presents a spectral analysis of the VC schemes for the linear transport equation. In Section 4, a grid convergence study is performed to validate the order of accuracy and the developed schemes are applied in the diagonal advection of a 2D isentropic vortex over very long distances. Finally, the consistency of the VC schemes with complex flow dynamics are evaluated in the computation of the viscous Taylor–Green Vortex and the results are discussed in Section 5.

2. High-order vorticity confinement schemes

2.1. One-dimensional scalar formulation

In the scalar case of the linear transport equation

$$\frac{\partial u}{\partial t} + c\,\frac{\partial u}{\partial x} = 0 \qquad with \quad c > 0 \tag{1}$$

the VC method will be simply referred to as 'confinement' since the transported variable does not specifically correspond to vorticity. Previous studies consisted in the investigation of confinement for high-order extensions of the Lax–Wendroff and Beam-Warming schemes [22,24]. In both of these cases an analysis of the space discretization is not straightforward as these schemes are coupled in space-time. The present study is therefore focusing on a decoupled family of schemes, based on high-order centered space discretizations.

Considering a uniform grid with spacing h ($x_j = j\,h,\ j \in \mathbb{Z}$), the convective derivative of Eq. (1) can be approximated at mth-order of accuracy using a linear flux discretization operator $\mathcal{R}^m$ of the generic conservative form:

$$\left.\frac{\partial(\bullet)}{\partial x}\right|_{x=x_j} = \frac{1}{h}\left(\mathcal{R}^m_{j+\frac{1}{2}}(\bullet) - \mathcal{R}^m_{j-\frac{1}{2}}(\bullet)\right) + \mathcal{O}(h^m)$$
$$= \frac{1}{h}\sum_{l=-k}^{r} a_l\,(\bullet)_{j+l} + \mathcal{O}(h^m) \tag{2}$$

where k, r define the stencil of the discrete operator and a_l are real constants. For standard centered discretizations, that is for $r = k$ and $a_l = -a_{-l}$, and using the discretization operators $\delta(\bullet)_{j+\frac{1}{2}} := (\bullet)_{j+1} - (\bullet)_j$ and $\mu(\bullet)_{j+\frac{1}{2}} := \frac{1}{2}((\bullet)_{j+1} + (\bullet)_j)$, the space approximation operator of Eq. (2) can be written at 8th-order of accuracy under the more compact form [25,26]:

$$\frac{\partial(\bullet)}{\partial x} = \frac{1}{h}\delta\mu\left(I - \frac{1}{6}\delta^2 + \frac{1}{30}\delta^4 - \frac{1}{140}\delta^6\right)(\bullet) + \mathcal{O}(h^8) \tag{3}$$

with I being the identity operator. The above discretization uses a 9-point stencil and results from recursive corrections of the leading truncation error term of a low-order discretization. The corresponding 6th, 4th and 2nd-order approximations can be obtained by recursively suppressing the δ^6, δ^4 and δ^2 terms. Since the operator of Eq. (3) is purely dispersive, explicit artificial dissipation is introduced to the discretization for stability. The dissipation operator is linear and can be written in the form:

$$\mathcal{D}^m_{j+\frac{1}{2}}(\bullet) = \delta\left(\delta^{m-2}\right)(\bullet) \tag{4}$$

The numerical flux of the space discretization at pth (odd)-order of accuracy then writes:

$$F^p_{j+\frac{1}{2}} = \mathcal{R}^p_{j+\frac{1}{2}}\left(u_j\right) - k_p\,\mathcal{D}^p_{j+\frac{1}{2}}\left(u_j\right)$$
$$\text{or} \quad F^p_{j+\frac{1}{2}} = \mu\left(\sum_{l=0}^{(p-1)/2} b_l\,\delta^{2l}\right)u_j - k_p\,\delta\left(\delta^{p-2}\right)u_j \tag{5}$$

where b_l are the coefficients of Eq. (3) and k_p is a real constant called the artificial dissipation coefficient. It is demonstrated in [25] that, for the specific choice $k_p = \frac{1}{2}\,b_{(p-1)/2}$, the numerical flux of Eq. (5) is equivalent to that of a non-compact upwind scheme. In that case, the discretization corresponds to the DNC (Directional Non-Compact) family of schemes derived by Lerat & Corre in [25], which are related to the MUSCL schemes of Van Leer based on Flux Extrapolation without limiters (FE-MUSCL).

The idea of confinement is to introduce an additional nonlinear negative dissipation operator to balance the excess dissipation of the baseline numerical scheme. The nonlinear dissipation of confinement can be written as the operator:

$$\mathcal{C}^m_{j+\frac{1}{2}}(\bullet) = \mathcal{D}^m_{j+\frac{1}{2}}\left(\tilde{h}(\bullet)\right) = \delta\left(\delta^{m-2}\right)\left(\tilde{h}(\bullet)\right)_j \tag{6}$$

which is referred to as the confinement term. Note that the operator of Eq. (6) is built on the same stencil as the operator $\mathcal{D}^m$ of Eq. (4), using the harmonic mean $\tilde{h}$ of the transported variable at each grid position, instead of the variable itself. The harmonic mean between two neighboring grid points is defined as:

$$\left(\tilde{h}(\bullet)\right)_j = \tilde{h}((\bullet)_j, (\bullet)_{j-1}) = \begin{cases} \frac{2(\bullet)_j(\bullet)_{j-1}}{(\bullet)_j + (\bullet)_{j-1}}, & \text{if} \quad (\bullet)_j(\bullet)_{j-1} > 0 \\ 0, & \text{otherwise} \end{cases} \tag{7}$$

Other possibilities exist besides the harmonic mean for the formulation of the confinement term [19,27], under the restriction that the function is nonlinear [16], but the investigation of such alternatives lies outside the scope of the present work.

The numerical flux of the space discretization with confinement can be written as a sum of baseline convective flux discretization,

artificial dissipation and the confinement term. At pth (odd)-order of accuracy this is:

$$F^p_{j+\frac{1}{2}} = \mathcal{R}^p_{j+\frac{1}{2}}\left(u_j\right) - k_p\,\mathcal{D}^p_{j+\frac{1}{2}}\left(u_j\right) + \varepsilon\,\mathcal{D}^p_{j+\frac{1}{2}}\left(\tilde{h}(u)\right)_j$$

$$\text{or}\quad F^p_{j+\frac{1}{2}} = \mu\left(\sum_{l=0}^{(p-1)/2} b_l\,\delta^{2l}\right)u_j - k_p\,\delta\left(\delta^{p-2}\right)u_j + \varepsilon\,\delta\left(\delta^{p-2}\right)\left(\tilde{h}(u)\right)_j \tag{8}$$

where the confinement term is multiplied by ε, which is a real constant called the confinement parameter. Since the operator $\mathcal{D}^m$ is linear and the coefficients k_p, ε are constant in space, the numerical flux of Eq. (8) can also be written in the more compact form:

$$F^p_{j+\frac{1}{2}} = \mathcal{R}^p_{j+\frac{1}{2}}\left(u_j\right) - \mathcal{D}^p_{j+\frac{1}{2}}\left(k_p\,u_j - \varepsilon\,(\tilde{h}(u))_j\right) \tag{9}$$

in which case the added computational cost of confinement is practically reduced to the cost of the calculation of the harmonic mean of Eq. (7).

The semi-discrete (continuous in time, discrete in space) conservative approximation of Eq. (1) is finally formulated as:

$$\frac{\partial u}{\partial t} + c\,\frac{1}{h}\left(F^p_{j+\frac{1}{2}} - F^p_{j-\frac{1}{2}}\right) = 0 \tag{10}$$

For the linear flux discretization of Eq. (5) the scheme will be referred to as the baseline pth-order FE-MUSCL scheme (FE-MUSCLp) whereas for the nonlinear flux discretization of Eq. (8) it will be referred to as the pth-order FE-MUSCL scheme with confinement (FE-MUSCLp-C).

The semi-discrete approximation of Eq. (10) can be equally represented by its equivalent partial differential equation, which is representative of the numerical error of the discretized problem. For the pth (odd)-order flux discretization of Eq. (8) this is written:

$$\frac{\partial u}{\partial t} + c\,\frac{\partial u}{\partial x} = c\,h^p\left(k_p\,\frac{\partial^{p+1}u}{\partial x^{p+1}} - \varepsilon\,\frac{\delta^{p+1}\left(\tilde{h}(u)\right)_j}{h^{p+1}}\right) + c\,b_{\frac{p+1}{2}}\,h^{p+1}\,\frac{\partial^{p+2}u}{\partial x^{p+2}} \tag{11}$$

where the harmonic mean has been kept intact for simplicity. Above, the leading truncation error term is of dissipative nature since the FE-MUSCL discretizations (5), (8) are odd-order accurate. This leading dissipation term is driven by the nonlinear balance between the operators $\mathcal{D}^m$ and $\mathcal{C}^m$. The second term of the right-hand side represents the leading dispersive error term, which comes from the discretization operator $\mathcal{R}^m$. Note however that the harmonic mean term is nonlinear and therefore its expansion yields mixed dispersive, dissipative and even singular error terms that cannot be straightforwardly analyzed [22]. This subject will be further addressed in Section 3.

A similar expression to Eq. (11) has been obtained for high-order extensions of the Lax–Wendroff scheme, thus indicating a similarity of the asymptotic solution analysis in [24] with the decoupled space discretization of the present work.

2.2. Euler/Navier–Stokes equations

In the original 1st-order VC2 formulation of Steinhoff, the Vorticity Confinement term is added in the momentum equation as a source term. The conservative differential form of the momentum conservation equation can then be written:

$$\frac{\partial \rho\vec{v}}{\partial t} + \vec{\nabla}\cdot\left(\rho\vec{v}\otimes\vec{v} + p\bar{\bar{I}} - \bar{\bar{\tau}}\right) = \vec{f} \tag{12}$$

with the Vorticity Confinement term:

$$\vec{f} = -\vec{\nabla}\times\left(\mu\,\vec{\omega} - \varepsilon\,\vec{\mathrm{w}}\right) \tag{13}$$

The first part is a linear artificial dissipation term with coefficient μ aligned with the vorticity vector $\vec{\omega} = \vec{\nabla}\times\vec{v}$. The second part is the negative dissipation confinement term with coefficient ε. This part is based on a vector $\vec{\mathrm{w}}$ with magnitude equal to the harmonic mean of the modulus of vorticity around the neighboring cells and aligned with vorticity as:

$$\vec{\mathrm{w}} = \frac{\vec{\omega}}{\|\vec{\omega}\|}\tilde{h}(\omega_j) = \frac{\vec{\omega}}{\|\vec{\omega}\|}N\left(\sum_{j=1}^{N}\|\vec{\omega}_j\|^{-1}\right)^{-1} \tag{14}$$

The introduction of an additional positive dissipation term in the VC formulation of Eq. (13) may appear counterintuitive. This linear dissipation is however different from the baseline scheme's dissipation in the sense that it is both explicitly based on vorticity and independent of the baseline method. It therefore gives more freedom in the adjustment of the strength of the VC term.

The analogy of Eq. (13) with the confinement formulation in the case of the linear transport equation can be revealed by taking the curl of the momentum equation (12) to derive the vorticity transport equation. By dividing with density we can obtain the specific vorticity transport equation, which in the case of a 2D isolated vortex in inviscid flow reduces to:

$$\frac{\partial(\vec{\omega}/\rho)}{\partial t} + \vec{v}\cdot\vec{\nabla}(\vec{\omega}/\rho) - \frac{1}{\rho}\vec{\nabla}^2(\mu\vec{\omega} - \varepsilon\vec{\mathrm{w}}) = 0 \tag{15}$$

$$\text{or}\quad \frac{\partial(\omega/\rho)}{\partial t} + \vec{v}\cdot\vec{\nabla}(\omega/\rho) - \frac{1}{\rho}\vec{\nabla}^2\left(\mu\omega - \varepsilon\tilde{h}(\omega_j)\right) = 0 \tag{16}$$

The contribution of the linear dissipation term of Eq. (13) to the vorticity transport equation is thus similar to the linear artificial dissipation $\mathcal{D}^m$ (see Eqs. (4) and (5)) in the linear transport equation. Furthermore, it has been shown that by ignoring the baseline scheme's dissipation, the asymptotic solutions of Eq. (16) are driven by the VC term and depend on the mesh size for given values of the confinement parameters, similarly to what is known for the asymptotic solutions of confinement for the linear transport equation [24].

By analogy with the δ operator in the linear scalar case, the curl operator can be recursively applied on the VC term of Eq. (13) to increase the order of differencing. By introducing the vector $\vec{\alpha} = -(\mu\vec{\omega} - \varepsilon\vec{\mathrm{w}})$ to simplify the equations and applying the curl operator twice on $\vec{f}$, we can introduce the equivalent of a fourth difference and obtain:

$$\vec{\nabla}\times\vec{f} = \vec{\nabla}\times\vec{\nabla}\times\vec{\alpha} = \vec{\nabla}\left(\vec{\nabla}\cdot\vec{\alpha}\right) - \vec{\nabla}^2\vec{\alpha}$$
$$\vec{f}_3 = \vec{\nabla}\times\vec{\nabla}\times\vec{f} = -\vec{\nabla}\times\left(\vec{\nabla}^2\vec{\alpha}\right) = \vec{\nabla}\times\left(\vec{\nabla}^2(\mu\vec{\omega} - \varepsilon\vec{\mathrm{w}})\right) \tag{17}$$

A 3rd-order extension of VC can therefore be obtained by taking the Laplacian of the original term. It is important to note that the Laplace operator is rotationally invariant and therefore consistent with the physics of isolated vorticity and the idea of the original VC method of Steinhoff. Furthermore, the alternate sign of higher-order derivative terms is naturally introduced by the recursive applications of the curl operator. The 5th-order VC term is then obtained by taking the bi-Laplacian of the VC term of Eq. (13):

$$\vec{f}_5 = \vec{\nabla}\times\vec{\nabla}\times\vec{f}_3 = \vec{\nabla}\times\left(\vec{\nabla}^4\vec{\alpha}\right) = -\vec{\nabla}\times\left(\vec{\nabla}^4(\mu\vec{\omega} - \varepsilon\vec{\mathrm{w}})\right) \tag{18}$$

Since the higher difference alone does not suffice, the use of undivided differences in the computation of the Laplace operator will ensure consistency with the original partial differential equation and provide increased order of accuracy. Note also that both the original VC and the higher-order extensions are independent from the choice of space discretization or time integration scheme. In three dimensions, the vector Laplacian of Eq. (17) writes:

$$\vec{\nabla}^2\vec{\alpha} = \vec{\nabla}\left(\vec{\nabla}\cdot\vec{\alpha}\right) - \vec{\nabla}\times\vec{\nabla}\times\vec{\alpha} \tag{19}$$

Provided that $\vec{\alpha}$ is a continuous function in space and for a Cartesian coordinate system, the vector Laplacian degrades to:

$$\vec{\nabla}^2\vec{\alpha} = \left(\nabla^2\alpha_x,\ \nabla^2\alpha_y,\ \nabla^2\alpha_z\right) \tag{20}$$

greatly reducing the complexity of its numerical calculation.

The analogy of Eq. (17) with Eq. (13), can be investigated by taking the curl of the developed scheme, which corresponds to the vorticity transport equation (16). In the case of an isolated 2D vortex in inviscid flow:

$$\begin{aligned}\vec{\nabla}\times\vec{f}_3 &= -\vec{\nabla}\times\left(\vec{\nabla}\times\vec{\nabla}^2\vec{\alpha}\right)\\ &= -\vec{\nabla}\vec{\nabla}\cdot\left(\vec{\nabla}^2(\mu\vec{\omega}-\varepsilon\vec{\mathrm{w}})\right)+\vec{\nabla}^2\left(\vec{\nabla}^2(\mu\vec{\omega}-\varepsilon\vec{\mathrm{w}})\right)\\ &= -\vec{\nabla}\vec{\nabla}\cdot\left(\vec{\nabla}\left(\vec{\nabla}\cdot\mu\vec{\omega}-\vec{\nabla}\cdot\varepsilon\vec{\mathrm{w}}\right)-\vec{\nabla}\times\vec{\nabla}\times(\mu\vec{\omega}-\varepsilon\vec{\mathrm{w}})\right)\\ &\quad+\vec{\nabla}^2\left(\vec{\nabla}^2(\mu\vec{\omega}-\varepsilon\vec{\mathrm{w}})\right)\\ &= \vec{\nabla}^2\left(\vec{\nabla}^2(\mu\vec{\omega}-\varepsilon\vec{\mathrm{w}})\right)\end{aligned} \tag{21}$$

since vorticity is perpendicular to the gradient of the harmonic mean of vorticity modulus for a 2D vortex. The new term is therefore analogous to the VC term of Eq. (15), expressed as the sum of a linear dissipation and a nonlinear negative dissipation term.

The VC2 formulation of Steinhoff is preferable to the original VC1 since it displays no singularity at the vortex core and is conservative. The latter is made clear by an application of the divergence theorem for the cross product of two sample real vector fields $\vec{q}$, $\vec{b}$, smooth in the neighborhood of a volume Ω bounded by a surface $S=\partial\Omega$:

$$\int_\Omega \vec{\nabla}\cdot(\vec{q}\times\vec{b})\ d\Omega = \oint_{\partial\Omega}(\vec{q}\times\vec{b})\cdot\vec{n}\ dS \tag{22}$$

where $\vec{n}$ is the unit vector normal to the boundary $\partial\Omega$. By performing a circular shift of the operands in both sides and, without loss of generality, assuming that the vector field $\vec{b}$ remains constant within the volume Ω we get:

$$\int_\Omega \vec{\nabla}\times\vec{q}\ d\Omega = \oint_S \vec{n}\times\vec{q}\ dS \tag{23}$$

which is a three-dimensional variation of the classical Kelvin–Stokes theorem. Applied to the volume integral of the VC source term of Eq. (13), Eq. (23) gives:

$$-\int_\Omega \vec{\nabla}\times(\mu\vec{\omega}-\varepsilon\vec{\mathrm{w}})\ d\Omega = -\oint_S \vec{n}\times(\mu\vec{\omega}-\varepsilon\vec{\mathrm{w}})\ dS \tag{24}$$

Finally, the integral form of the Navier–Stokes momentum equation writes:

$$\begin{aligned}&\frac{\partial}{\partial t}\int_\Omega \rho\vec{v}\ d\Omega + \oint_S \rho\,\vec{v}(\vec{v}\cdot\vec{n})\ dS + \oint_S p\cdot\vec{n}\ dS - \oint_S \bar{\bar{\tau}}\cdot\vec{n}\ dS\\ &\quad= -\oint_S \vec{n}\times(\mu\vec{\omega}-\varepsilon\vec{\mathrm{w}})\ dS\end{aligned} \tag{25}$$

in which case VC can be assimilated within the surface integral alongside physical fluxes as:

$$\begin{aligned}&\frac{\partial}{\partial t}\int_\Omega \rho\vec{v}\ d\Omega + \oint_S[(\rho\,\vec{v}\otimes\vec{v}+p\bar{\bar{I}}-\bar{\bar{\tau}})\cdot\vec{n}\\ &\quad-(\mu\vec{\omega}-\varepsilon\vec{\mathrm{w}})\times\vec{n}]\,dS = 0\end{aligned} \tag{26}$$

Eq. (26) demonstrates that the VC2 formulation is equivalent to a nonlinear anti-diffusive flux correction applied in vortical regions. In principle, this is not so different from the idea of limited downwind fluxes or anti-dissipative flux corrections applied for the sharpening of contact discontinuities [28,29], but for the case of VC it is explicitly formulated for vorticity rather than the approximation of convective terms. It naturally follows from Eqs. (17) and (18) that the same property stands for the high-order VC extensions.

2.3. Numerical implementation

The Vorticity Confinement schemes presented in Section 2.2 were integrated into the DynHoLab solver of the DynFluid laboratory [30] up to 5th-order of accuracy. The in-house code solves the Euler and Navier–Stokes equations in a Finite Volume approach.

Physical fluxes are separated in an inviscid and a viscous part, and discretized separately for each direction. Setting $W=(\rho,\ \rho\vec{v},\ \rho E)^T$ the state vector of conservative variables and $f_d=f_d(W)$ the inviscid flux vector in the dth space direction, inviscid flux derivatives are approximated using the centered approximations of Eq. (3) [25,26] and the damping of spurious oscillations is achieved by introducing a high-order dissipation term. The 1st-, 3rd- and 5th-order numerical fluxes are respectively written:

$$\begin{aligned}\mathcal{F}^d_{j+\frac{1}{2}} &= \mu_d f_d - \frac{1}{2}|Q_d|\delta_d W\\ \mathcal{F}^d_{j+\frac{1}{2}} &= \left(I-\frac{1}{6}\delta_d^2\right)\mu_d f_d - \frac{1}{12}|Q_d|\delta_d^3 W\\ \mathcal{F}^d_{j+\frac{1}{2}} &= \left(I-\frac{1}{6}\delta_d^2+\frac{1}{30}\delta_d^4\right)\mu_d f_d - \frac{1}{60}|Q_d|\delta_d^5 W\end{aligned} \tag{27}$$

where δ_d and μ_d are respectively the difference and average operators and $|Q_d|$ a dissipation matrix taken as the Roe average matrix in direction d. For Navier–Stokes calculations, viscous fluxes are approximated on cell face centers using a standard 3-point compact formula that is 2nd-order accurate on regular Cartesian grids. Gradients ∇W are directly calculated on cell face centers by applying a standard Gauss divergence theorem on shifted cells. As the space discretization schemes of Eq. (27) are equivalent to a high-order MUSCL reconstruction based on Flux Extrapolation, in the following they will be referred to as FE-MUSCL schemes, in analogy with the flux discretizations of Eq. (5) for the scalar transport equation.

For the periodic flows investigated in this article, domain/zone boundaries are treated by introducing layers of ghost cells to expand the computational domain in each mesh direction. This way boundary fluxes can be approximated using the same large-stencil centered schemes as in the interior of the domain.

The Vorticity Confinement term of Eqs. (13) and (17) is added to the right-hand side of the momentum equation as a source term. For high-order VC, the Laplace operator is computed with a 5-point scheme using undivided differences to ensure the increased order of accuracy. Gradients are calculated at cell centers and consequently the Laplacian of Eq. (20) is calculated from a Gauss divergence theorem based on arithmetic average reconstructions of the gradients from the adjacent cell centers. A 3-point stencil similar to the one used for the calculation of viscous fluxes could also be used but the 5-point scheme is more computationally efficient and we have found that it is more accurate on coarse meshes. The calculation of vorticity and Laplacian/bi-Laplacian is performed successively in the extended computational domain, starting from the outer ghost cell layer and towards the domain interior, so that the VC term is accurately computed on the domain boundary.

The confinement parameters μ,ε are not varying in space or time and are multiplied by the mesh size for consistency. In the presentation of results it has been chosen to express the confinement parameters as ε, μ/ε as the first is a measure of the intensity of the confinement part and the second represents the ratio between explicit artificial dissipation and confinement within the VC term. Note that under this notation, it is the value of ε that defines the magnitude of the VC flux correction. The selection of these parameters is done on a trial-and-error basis but is quite straightforward. Being the coefficient of an artificial dissipation that is added to that of the baseline scheme in vortical regions, the value of μ should be kept to a minimum, and even set to zero, when possible.

It might however be the case that the dissipation of some baseline schemes is not enough to balance the nonlinear negative dissipation part of VC, or that the numerical dissipation of the baseline scheme is not explicitly known. In such cases a small nonzero value of μ can be used to introduce some stabilizing rotational dissipation in vortical regions. For the dissipative FE-MUSCL schemes used in the present work, we have found that the value of μ can generally be set to zero without sacrificing the scheme's robustness, and further reducing dissipation for the same values of ε. In the following, we are however mainly presenting results for $\mu > 0$, for consistency with previous studies using VC in the literature. On the other hand, the confinement parameter ε plays a major role in adjusting the magnitude of VC to the dissipation error of the baseline flux discretization. For schemes with explicitly known artificial dissipation, the value of ε is usually chosen to be of the order of magnitude of the artificial dissipation coefficient. The choice of the confinement parameters is further discussed in Section 4.2 by means of a parametric study.

The vortical flow regions, where VC is applied, are selected based on a minimum cut-off value of the Q-criterion [31]. However, as the fine selection of vortical regions to apply VC is not simple for realistic flows, the aim of this cut-off value is mainly to avoid the creation of unphysical vorticity concentration in irrotational flow regions. Multiple alternative identification criteria exist but the Q-criterion is computationally efficient and was found to be adequate for the cases investigated in this article. Its cut-off value was set to 0.1 for all presented computations. Finally, since the nonlinear VC correction should be applied in clearly defined vortical regions, the cut-off is complemented by deactivating VC if vorticity changes sign between neighboring cells, in analogy with the harmonic mean definition (7) in the scalar case.

3. Spectral analysis for the scalar case

This section consists in an evaluation of the dispersive and dissipative error of the schemes presented in Section 2.1 in the wavenumber space. The wave propagation properties of these schemes are evaluated analytically using linear theory and by means of a quasi-linear numerical method. It is reminded that for scalar transport cases confinement is formulated without the use of additional positive artificial dissipation, i.e. without a μ term, as its role is explicitly taken by the baseline artificial dissipation (Eq. (9)).

3.1. Linear analysis

General sinusoidal solutions of the continuous Eq. (1) are:

$$u_{e,k}(x,t) = \hat{u}_k(0)\, e^{ik(x-ct)} \tag{28}$$

where k is the wavenumber and $\hat{u}_k(t)$ is the solution amplitude. The subscript e is used to denote the exact solution of the linear transport equation. On a discrete uniform grid with spacing h ($x_j = jh,\ j \in \mathbb{Z}$) this exact solution is written:

$$u_{e,k}(x_j,t) = \hat{u}_k(0)\, e^{i\xi\left(j-\frac{ct}{h}\right)} = \hat{u}_k(0)\, e^{-i\frac{ct}{h}\xi}\, e^{ij\xi} \tag{29}$$

where $\xi = kh$ is the assigned reduced wavenumber. We can then proceed for the semi-discrete Eq. (10), written under a single space approximation operator $\mathcal{S}(\bullet)$ as:

$$\frac{\partial u}{\partial t} = \mathcal{S}\left(u_j\right) = -\frac{c}{h}\left(F^p_{j+\frac{1}{2}} - F^p_{j-\frac{1}{2}}\right) \tag{30}$$

A discrete harmonic:

$$u_k(x_j,t) = \hat{u}_k(t)\, e^{ij\xi} \tag{31}$$

is a solution of the semi-discrete Eq. (30) when:

$$\frac{\partial \hat{u}_k(t)}{\partial t} = \Omega(\xi)\hat{u}_k(t) \Longleftrightarrow \hat{u}_k(t) = \hat{u}_k(0)\, e^{\Omega(\xi)t} \tag{32}$$

where $\Omega(\xi)$ is the Fourier symbol (or equivalently the eigenvalues) of the space discretization. For an explicit space discretization operator $\mathcal{S}(\bullet)$, i.e. for an explicit flux discretization $F^p_{j+\frac{1}{2}}$, the Fourier symbol results from [26,32]:

$$\Omega(\xi)\, e^{ij\xi} = \mathcal{S}\left(e^{ij\xi}\right) \tag{33}$$

Using Eq. (33), Eq. (32) gives the complex amplitude for which the harmonic (31) is a solution of Eq. (30):

$$\hat{u}_k(t) = \hat{u}_k(0) e^{\left[\mathcal{S}\left(e^{ij\xi}\right)/e^{ij\xi}\right]t} \tag{34}$$

expressed through the space discretization operator. If the operator $\mathcal{S}(\bullet)$ is linear, the amplitude can be expressed through the modified wavenumber $\xi^* = \xi^*(\xi)$ of the space discretization as:

$$\hat{u}_k(t) = \hat{u}_k(0) e^{-i\frac{ct}{h}\xi^*} \tag{35}$$

The semi-discrete solution (31) then writes:

$$u_k(x_j,t) = \hat{u}_k(0)\, e^{-i\frac{ct}{h}\xi^*}\, e^{ij\xi} \tag{36}$$

From a comparison with the exact solution (29) it is clear that the modified wavenumber ξ^* expresses the differencing error of the space discretization in the wavenumber space. The equivalent of Eq. (36) for the Fourier symbol Ω can be obtained if the amplitude $\hat{u}_k(t)$ is expressed directly using Eq. (32).

The modified wavenumber for linear space discretization schemes can be derived by following the above procedure and writing the semi-discrete solution in the form of Eq. (36). It is not straightforward though to do the same for schemes with confinement, because the confinement term in Eqs. (6) and (8) is intrinsically non-linear. Confinement schemes can however be linearized using exponent functions, which behave like eigenfunctions for the harmonic mean on a uniform grid. For a single harmonic on a uniform grid with spacing h ($x_j = jh,\ j \in \mathbb{Z}$) and a time step Δt ($t = n\Delta t,\ n \in \mathbb{Z}$) the harmonic mean is written:

$$\tilde{h}(u^n)_j = \tilde{h}(u^n_j, u^n_{j-1}) = \left[\frac{1}{2}\left(\frac{1}{u^n_j} + \frac{1}{u^n_{j-1}}\right)\right]^{-1} = 2\left(1+e^{i\xi}\right)^{-1} u^n_j \tag{37}$$

where $u^n_j = u_k(x_j,t) = \hat{u}_k(t)e^{ij\xi}$ and the factor $2\left(1+e^{i\xi}\right)^{-1}$ is independent of the position on the computational grid. Taking advantage of Eq. (37), the flux discretizations of Eq. (8) can be now written in the form Eq. (36).

The resulting modified wavenumber ξ^* of the pth-(odd) order FE-MUSCL flux discretization with confinement (FE-MUSCLp-C) of Eq. (8) can be expressed through the recurrence relation:

$$\begin{aligned}\xi^*_p(\xi) = & \sum_{l=0}^{(p-1)/2} b_l \left(\sum_{q=1}^{l+1} \eta_{l,q} \sin(q\,\xi)\right) \\ & + i\,2^{\frac{p+1}{2}} (-1)^{\frac{p+3}{2}} k_p (\cos\xi - 1)^{\frac{p+1}{2}} \\ & + 2^{\frac{p+1}{2}} (-1)^{\frac{p+1}{2}}\, \varepsilon\, \sin\xi \frac{(\cos\xi-1)^{\frac{p+1}{2}}}{\cos\xi+1} \\ & + i\,2^{\frac{p+1}{2}} (-1)^{\frac{p+1}{2}}\, \varepsilon\, (\cos\xi - 1)^{\frac{p+1}{2}}\end{aligned} \tag{38}$$

where b_l are the coefficients of Eqs. (3) and (5) and η are the real coefficients of the expanded centered difference operators of Eq. (3), given by:

$$\delta\mu\left(\delta^m(\bullet)_j\right) = \sum_{q=1}^{1+(m/2)} \eta_{m,q}\,(\bullet)_{j+q} - \eta_{m,q}\,(\bullet)_{j-q} \tag{39}$$

and presented in Table 1. Note that since the FE-MUSCL schemes are decoupled in space and time, the modified wavenumber is independent of the time step or the CFL number. The first term in

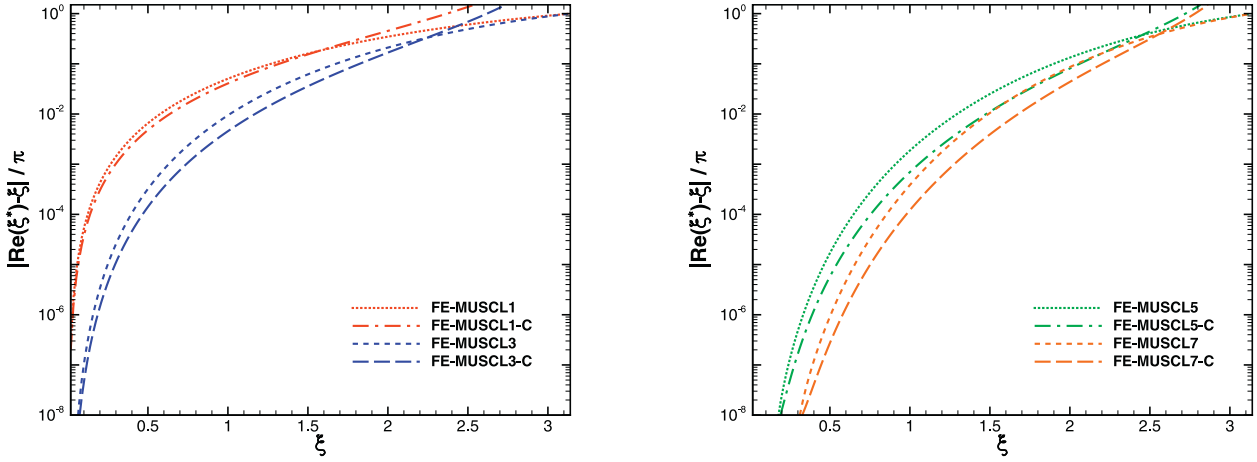

Fig. 1. Dispersion error of FE-MUSCL schemes up to 7th-order with and without confinement for $\varepsilon = 1.14\,k_p$.

Table 1
Coefficients $\eta_{m,q}$ in Eq. (39).

m	$q=1$	$q=2$	$q=3$	$q=4$
0	1			
2	−2	1		
4	5	−4	1	
6	−14	14	−6	1

Eq. (38) corresponds to the centered space discretization operator $\mathcal{R}^m$, the second to the explicit artificial dissipation operator $\mathcal{D}^m$ and the last two correspond to the nonlinear confinement $\mathcal{C}^m$. By suppressing the terms associated with ε in Eq. (38), the expression of ξ^* for the baseline pth-order FE-MUSCL flux discretizations of Eq. (5) is recovered.

Since the exact solution corresponds to $\xi^* = \xi$, $|Re(\xi^*) - \xi|/\pi$ can be used as a measure of dispersion or phase approximation error and $Im(\xi^*)$ can be used as a measure of dissipation error of the flux discretizations of Eqs. (5) and (8) compared to the exact solution.

Eq. (38) demonstrates that dissipation derives only from the artificial dissipation and confinement terms. It also shows that the nonlinear character of the confinement term produces an additional effect on the dispersion error of the scheme, i.e. $Re(\xi^*)$, even though the operator $\mathcal{C}^m$ is originally based on an even difference.

Fig. 1 compares the dispersive properties of FE-MUSCL-C confinement schemes with the corresponding baseline FE-MUSCL schemes up to 7th-order of accuracy. The confinement parameter is taken $\varepsilon = 1.14\,k_p$ for all cases, a value which is commonly used in the literature, but similar trends are obtained for values of ε at the same order of magnitude. The sensitivity to this choice is smaller at higher orders of accuracy, as k_p is smaller in this case (see Section 2.1). FE-MUSCL schemes with confinement are shown to have decreased phase approximation error compared to their linear counterparts at least up to the grid resolvability limit $\xi = \pi/2$ for all orders of accuracy.

However, Eq. (38) depicts the effect of confinement on dissipation as equivalent to a linear artificial dissipation, the nonlinear effect appearing only in phase approximation. As a result, FE-MUSCL schemes with confinement are predicted as unstable since the confinement parameter is taken $\varepsilon > k_p$ to ensure that the numerical scheme is globally anti-dissipative and therefore $Im(\xi^*) > 0$. This however is not in agreement with extensive numerical experiments, which have verified the stability of confinement schemes [22,27,33]. This discrepancy might be a result of the linearization of Eq. (37), which permits the application of linear stability theory, but does not appear to accurately represent the nonlinear mechanism of the scheme.

3.2. Numerical quasi-linear analysis

The following step is the evaluation of the numerical error of the schemes of Section 2.1 using a quasi-linear approach. It was originally applied by Pirozzoli [34] for the study of non-linear shock capturing schemes and was shown to produce an improved prediction compared to conventional analyses, providing results in general agreement with observations from their application in numerical experiments.

Again, we consider sinusoidal monochromatic initial conditions of the type $u_\xi(x_j,t) = \hat{u}_\xi(t)\,e^{ij\xi}$ for Eq. (1) on a uniform grid with spacing h ($x_j = jh$, $j \in \mathbb{Z}$). For all reduced wavenumbers ξ in the range $[0-\pi]$ that result in periodic initial conditions of this type on the computational grid, the numerical scheme is used to advance the initial signal to a very small time τ. For a harmonic of the type (31) and for time τ sufficiently small to exclude time integration error and ensure that the initial conditions remain monochromatic at the end of the calculation, the Discrete Fourier Transform (DFT) $\overline{u}$ is the complex amplitude (35) of the computed solution:

$$\overline{u_\xi}(x_j,\tau) = \hat{u_\xi}(0)\,e^{-i\frac{c\tau}{h}\xi^*} \tag{40}$$

It follows that $\overline{u_\xi}(x_j,0) = \hat{u_\xi}(0)$. Then, for time τ corresponding to a single time step, a modified wavenumber can be derived as:

$$\xi^*(\xi) = -\frac{1}{i\sigma}\ln\left(\frac{\overline{u_\xi}(x_j,\tau)}{\overline{u_\xi}(x_j,0)}\right) \tag{41}$$

where $\sigma = c\,\Delta t/h$ is the CFL number. For an unlimited computational domain, or periodic boundary conditions, this approach includes the nonlinear characteristics of the space discretization, but cannot predict any nonlinear mode interactions occurring at later times [34]. A comparison of the numerical approach with linear theory is presented in Fig. 2 as validation. Since the prediction of Eq. (38) is exact for linear schemes, the results of the two methods are in excellent agreement, in the complete wavenumber range. Very similar results were obtained for the confinement schemes based on high-order extensions of the Lax–Wendroff scheme of [22], since the time-coupled terms of these schemes diminish for a very small value of the CFL number. Fig. 2 also shows that results of the numerical spectral analysis for confinement schemes are not smooth in the complete wavenumber range. Specifically, 'spikes' are observed for $\xi \in \mathrm{P} = \{\pi/2,\ 3\pi/4,\ 4\pi/5,\ 9\pi/10\}$, wavenumbers equal or greater than the grid resolvability limit $\pi/2$ posed by

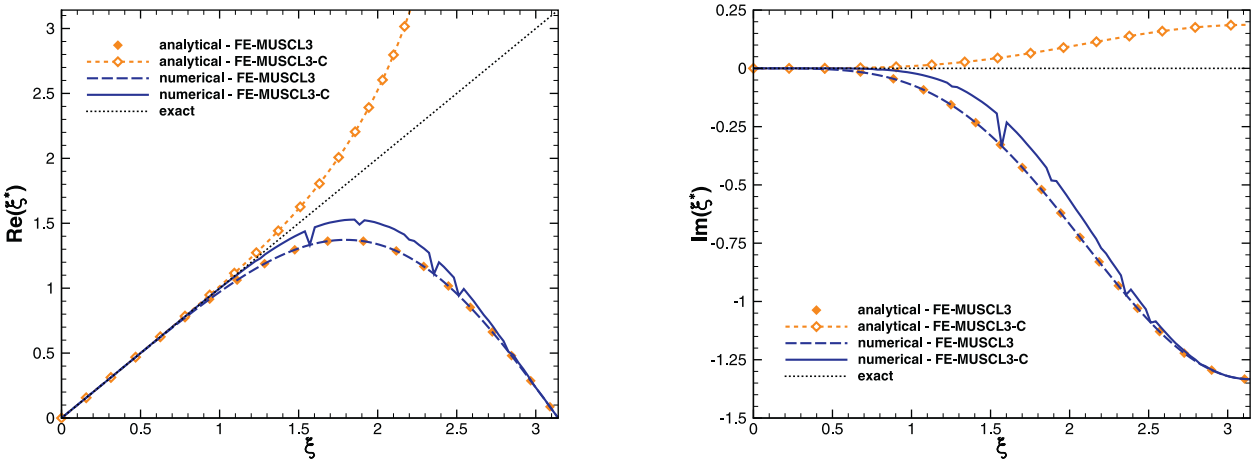

Fig. 2. Comparison of numerical spectral analysis with linear analytical theory. Baseline FE-MUSCL3 scheme and with confinement ($\varepsilon = 1.14\,k_p$).

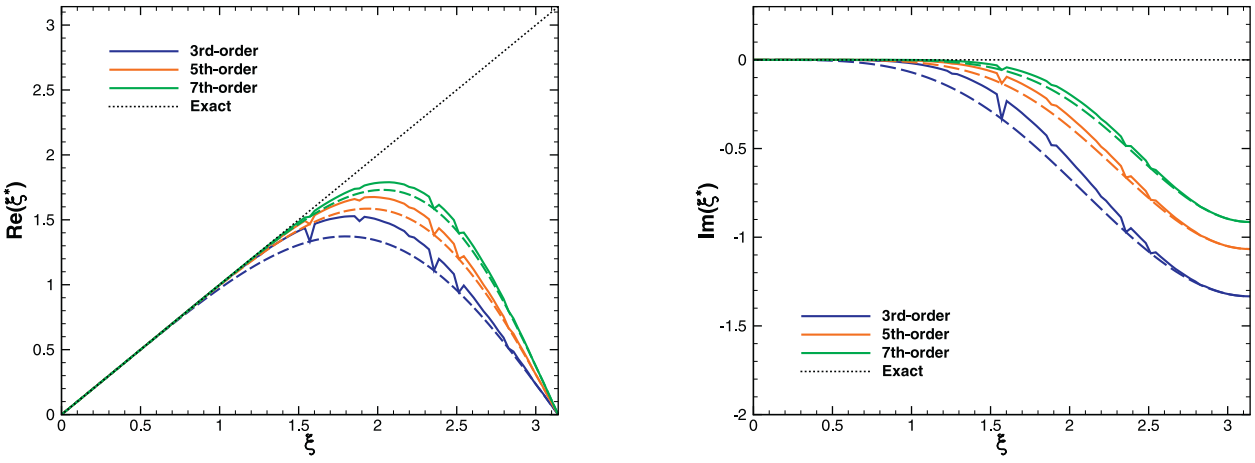

Fig. 3. Spectral properties of FE-MUSCL schemes up to 7th-order. Baseline schemes (dashed lines) and with confinement (solid lines), $\varepsilon = 1.14\,k_p$.

the Nyquist–Shannon theorem. For wavenumbers of the set P, the initial condition is such that the harmonic mean definition of Eq. (7) results to $\tilde{h}(u_j, u_{j-1}) = 0 \quad \forall j \in \{0, 1, \ldots, N\}$, in which case the total contribution of confinement vanishes and the flux discretization of Eq. (8) degrades to the baseline FE-MUSCL of Eq. (5). This weakness of confinement however refers to single harmonics and has not been observed in general problems, since frequencies higher than $\pi/2$ are under-resolved and should in any case be damped by the numerical scheme's inherent dissipation.

Spectral analysis results of the numerical method are presented in Fig. 3 for high-order FE-MUSCL schemes with and without confinement up to 7th-order of accuracy. Naturally, higher-order schemes are shown to provide a good approximation of the exact solution for a longer range of wavenumbers. More importantly, Fig. 3 shows that schemes with confinement are stable and that the benefit of the confinement flux correction is carried on to higher orders, with its effect being smaller as the order increases, in line with the reduced dissipation error of the baseline scheme. The improvement in terms of phase approximation is not obvious, as the confinement term of Eq. (8) is originally a dissipative operator, but is again attributed to the nonlinear properties of the term. It has been observed that optimized schemes in the wavenumber space achieve increased resolution at higher frequencies at the expense of higher dispersion error compared to standard schemes at very low wavenumbers [35], but the reduction of dispersion error for schemes with confinement appears in the complete wavenumber range. It should be however noted that slightly positive $Im(\xi^*)$ values are observed for schemes with confinement at very low frequencies, but after some time steps they are quickly compensated either by the nonlinear balance of the artificial dissipation and confinement terms, either by the dissipation of the time integration method. Furthermore, the schemes with confinement have improved dispersive and dissipative properties compared to their linear counterparts with the exception of wavenumbers $\xi \in \mathrm{P}$ where their spectral properties are reduced to those of the baseline scheme. Confinement can also achieve the preservation of waves over arbitrarily long distances [22,24], a non-linear property which is not taken into account by the present analysis but cannot be achieved even for high-order baseline schemes. Finally, the negative dissipation introduced by confinement does not affect the damping of the shortest wavelength $\xi = \pi$, which is associated to grid-to-grid oscillations.

The accuracy of the numerical schemes can be quantified by comparing their resolvability limit in the wavenumber space, or equivalently by computing the maximum wavenumber ξ_n for which the scheme approximates the exact solution under a defined error threshold E. In turn, this reduced wavenumber is equivalent to a minimum number of grid points per wavelength λ_n/h to ensure the accurate approximation of Eq. (1). Tables 2–3 show the effect of confinement on the resolvability limit of FE-MUSCL schemes due to dispersion and due to dissipation. The FE-MUSCL schemes of Eq. (5) are odd-order accurate and there-

Table 2
Resolvability limit due to dispersion for FE-MUSCL schemes ($E = 10^{-3}$).

	baseline		confinement	
	ξ_n	λ_n/h	ξ_n	λ_n/h
FE-MUSCL3	0.471	13.33	0.974	6.45
FE-MUSCL5	0.754	8.33	1.005	6.25
FE-MUSCL7	0.974	6.45	1.131	5.56

Table 3
Resolvability limit due to dissipation for FE-MUSCL schemes ($E = 10^{-3}$).

	baseline		confinement	
	ξ_n	λ_n/h	ξ_n	λ_n/h
FE-MUSCL3	0.314	20.00	0.660	9.52
FE-MUSCL5	0.628	10.00	0.848	7.41
FE-MUSCL7	0.880	7.14	1.037	6.06

fore have a leading truncation error term of dissipative nature, the accuracy limit being in turn defined by their dissipation error, rather than dispersion. Confinement is shown to achieve a considerable improvement of this limit due to dissipation, halving the minimum number of points per wavelength for the FE-MUSCL3 scheme and extending the well-resolved wavenumber range even for the more precise FE-MUSCL5/FE-MUSCL7. Interestingly, the FE-MUSCL3-C scheme exhibits even better 1D resolvability properties than a third-order (residual-based) compact scheme [36]. The 5th and 7th-order schemes with confinement tend toward the resolvability limits of the compact schemes of the same order. Furthermore, confinement is shown to improve phase approximation errors by an amount comparable to the improvement in terms of dissipation, even though the method had not been designed for this purpose.

It can be argued that, having a higher cut-off wavenumber both in terms of dispersion and dissipation, the FE-MUSCL3-C scheme is a preferable choice over the baseline FE-MUSCL5. This is true for $\xi < \xi_n$, but not representative of the complete wavenumber range, where the FE-MUSCL5 shows overall superior properties (Fig. 3). Furthermore, spectral analysis represents only wave propagation properties and not the improved approximation of the convective derivative provided by the FE-MUSCL5 scheme. Confinement is not equivalent to a correction of the leading truncation error term but represents a conservative correction to the baseline scheme allowing the accurate calculation of wave advection over arbitrarily long distances. This makes confinement an interesting method for approaching advection problems dominated by diffusion, but it is not capable of preserving structures not captured by the baseline scheme.

3.3. Time integration

Flux discretizations with confinement were shown to be stable by means of a quasi-linear numerical method, but this does not convey sufficient information on the stability and dispersive properties of the fully discrete equation. This subsection evaluates the stability of fully discrete schemes combining the flux discretizations of Eqs. (5) and (8) with classical Runge–Kutta methods for time integration.

The stability of a complete numerical scheme is evaluated by investigating whether the Fourier symbol of the space discretization lies within the stability region of the time integration method. The Fourier symbol Ω results from Eq. (33) and is related to the modified wavenumber of Eq. (36) as:

$$\Omega\Delta t = -i\,\sigma\,\xi^* \tag{42}$$

The Fourier symbol of the space discretization can therefore be obtained from Eq. (42) using the modified wavenumber obtained by the numerical method of Section 3.2. For the present analysis we consider the family of classical explicit low-storage Runge–Kutta (RK) algorithms:

$$\begin{aligned} u^{(0)} &= u^n \\ u^{(q)} &= (1 + d_q\Delta t)\,R\left(u^{(q-1)}\right) \\ u^{n+1} &= u^{(k)} \end{aligned} \tag{43}$$

for $q = 1, \ldots, k$. Above, d_q are the RK scheme coefficients and R is the right hand side of the original differential equation $\frac{du}{dt} = R(u)$. For linear partial differential equations, the amplification factor G of classical k-stage RK algorithms (RKk) is equal to the exact amplification factor:

$$G_{exact} = 1 + \sum_{j=1}^{\infty} \frac{(\Omega\Delta t)^j}{j!} \tag{44}$$

up to the kth-order term and in turn means that the scheme is kth-order accurate for linear problems. In turn, its stability region is defined by prescribing $|G| \leq 1$. Fig. 4 shows the stability region of RK algorithms against the Fourier symbol of FE-MUSCL schemes with and without confinement. Both FE-MUSCL and FE-MUSCL-C schemes remain within the stability region of RK3 and RK4 under the CFL condition. Note that for the pure centered discretizations of Eq. (3) the eigenvalues are located on the imaginary axis, therefore the dissipation is attributed only to the artificial dissipation and confinement term.

A sensitivity study to the values of the *CFL* number and the confinement parameter ε is presented in Fig. 5. The eigenvalues of the space discretization with confinement remain within the stability region of RK3/RK4 algorithms for a wide range of values of σ, and show small sensitivity to the choice of the confinement parameter.

4. Application of the method

4.1. Evaluation of the order of accuracy

The first validation case is a grid convergence study of a static 2D vortex. The evolution of the flow is computed based on the Euler equations, meaning that any spreading and diffusion originate from the dissipation of the numerical scheme. The isentropic vortex is initialized on a flow at rest using the model proposed by Yee et al. [37], which is an exact steady solution of the Euler equations.

Computations are performed on a square Cartesian mesh $(x, y) \in [-5, 5] \times [-5, 5]$ where the vortex is initialized at the center of the computational domain at $x_0 = y_0 = 0$. Different meshes of varying density were considered, ranging from $\Delta x = 0.4$ (625 cells) for the coarsest mesh to $\Delta x = 0.025$ (160000 cells) for the finest mesh with Δx being halved between two successive cases. Periodicity conditions were imposed on each side of the computational domain. Computations were run from $t = 0$ to $t = 1$ using a fixed ratio of $\frac{\Delta t}{\Delta x} = 2 \cdot 10^{-4}$ for all cases, to minimize any error introduced by time integration. Space discretization is performed using the FE-MUSCL schemes presented in Section 2.3, of order of accuracy ranging from 1st to 5th and time integration is performed using a classical 4-step Runge–Kutta algorithm. For cases where VC is applied, the order of accuracy shows very little sensitivity to the values of the confinement parameters. For the results presented in this section, these were set to $\mu/\varepsilon = 0.4$, $\varepsilon = 0.02$.

The computed solution is compared to the initial isentropic field and the L^2 norm of entropy error is computed based on the cell-averaged solution at cell centers. Fig. 6(a) shows the convergence of the L^2 norm of the error for baseline FE-MUSCL schemes

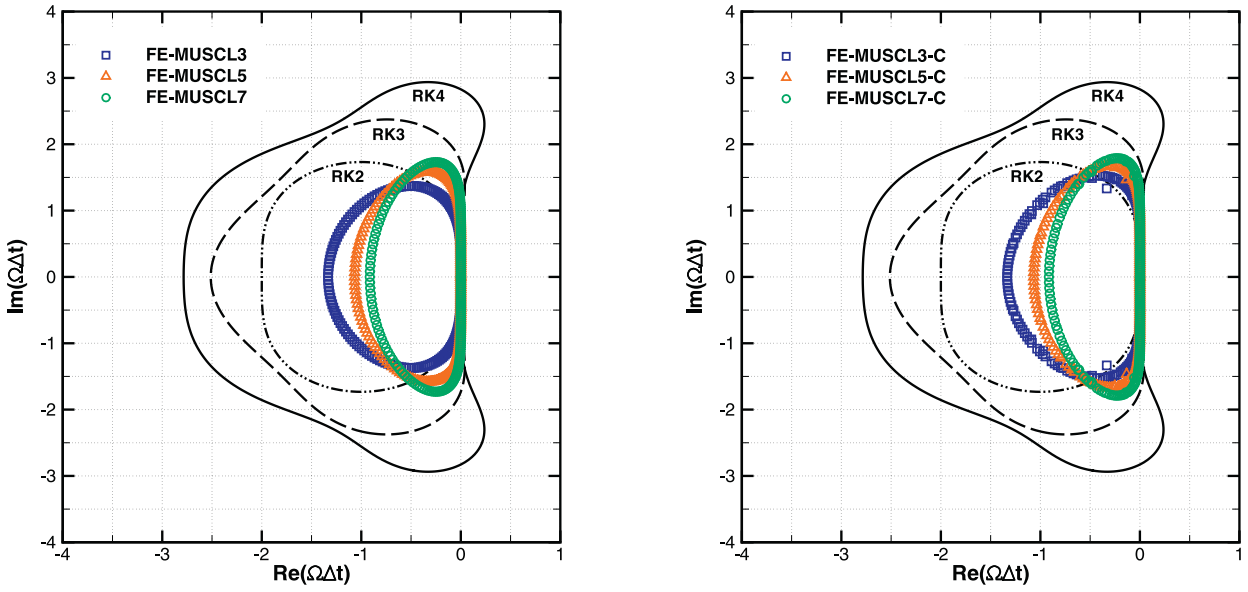

(a) FE-MUSCL (b) FE-MUSCL-C

Fig. 4. Stability region of classical Runge–Kutta algorithms and Fourier symbol of FE-MUSCL and FE-MUSCL-C space discretizations for $\sigma = 1.0$, $\varepsilon = 1.14\,k_p$.

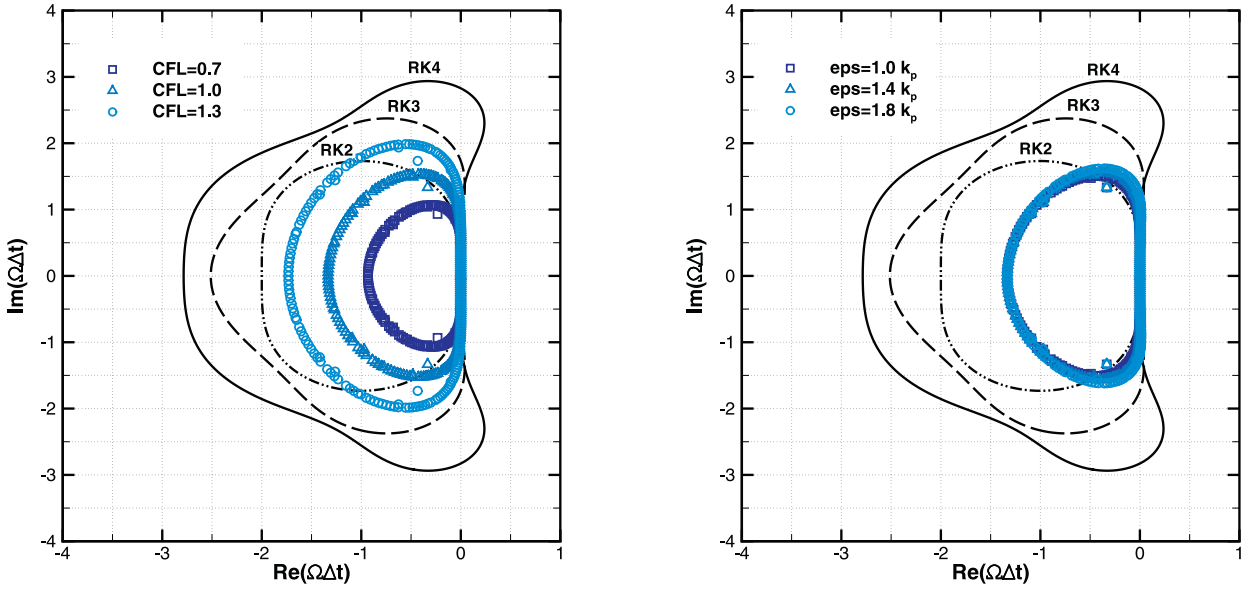

(a) Sensitivity to σ for $\varepsilon = 1.14\,k_p$ (b) Sensitivity to ε for $\sigma = 1.0$

Fig. 5. Sensitivity to the value of the *CFL* number and the confinement parameter for the FE-MUSCL3-C scheme.

of 1st, 3rd and 5th-order of accuracy. The error decreases according to the nominal convergence slope for all baseline schemes. Fig. 6(b) underlines the incompatibility of the original VC method with higher-order schemes, as the numerical error of the VC term dominates the solution, resulting in a 1st-order convergence slope regardless of the underlying scheme. Furthermore, Figs. 6(c) and 6(d) show that high-order VC extensions allow to recover the nominal order of accuracy. Details of the error convergence are presented in Table 4 for VC of the same order as the baseline scheme. VC is shown to reduce the absolute values of error up to 3rd-order of accuracy. Even though the absolute error values with VC are slightly higher at 5th-order, the nominal order of accuracy is always comparable to the one of the baseline scheme.

4.2. Diagonal vortex advection

The FE-MUSCL schemes used in the present work, as well as the majority of numerical schemes in general, are directional, meaning that numerical error is increased when the grid is not aligned with the direction of advection. The second test case is the advection of a 2D vortex in an inviscid uniform flow inclined by 45° with respect to the grid, so as to underline the effect of numerical error of both the baseline and the VC method.

The advection is studied on a square computational domain $(x, y) \in [-15, 15] \times [-15, 15]$. The nondimensional flow velocity components are $u = v = 1$ so that $|\vec{U}| = \sqrt{2}$ in the diagonal direction and the fluid variables are $\gamma = 1.4$, $p_{inf} = 1/\gamma$, $\rho_{inf} = 1$. The

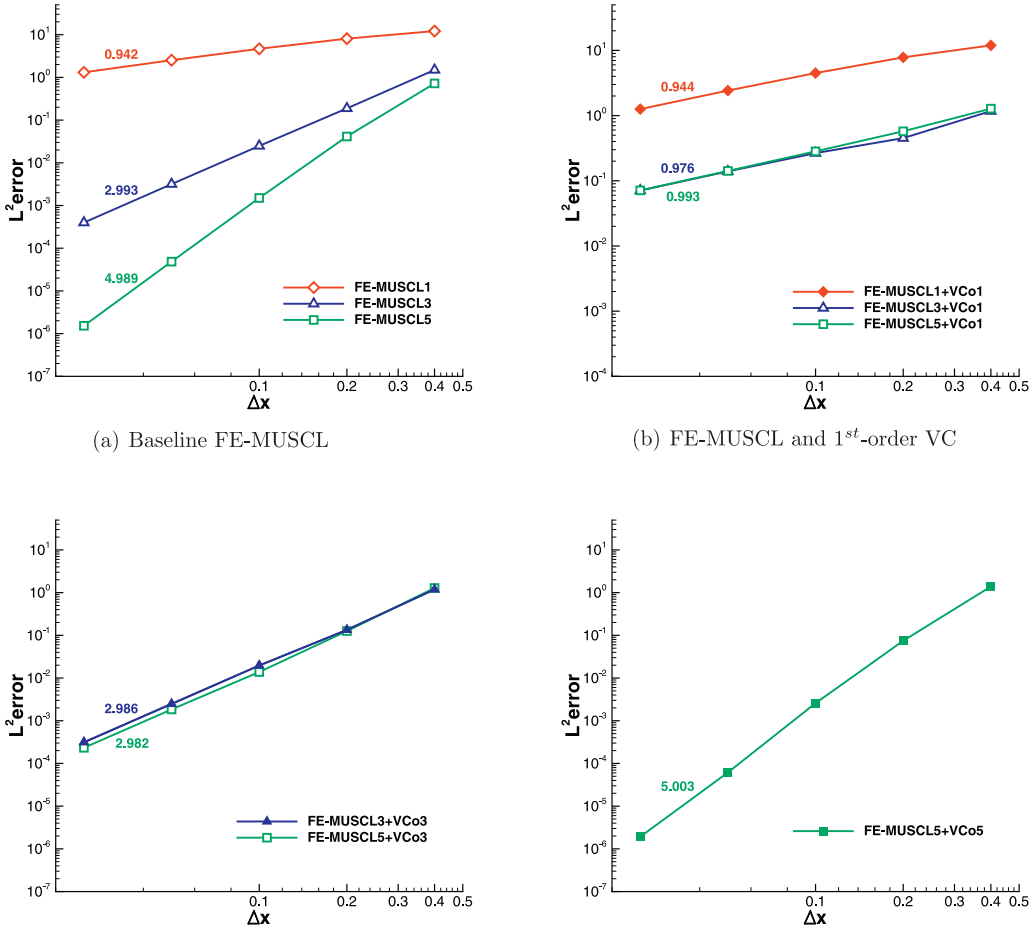

(a) Baseline FE-MUSCL

(b) FE-MUSCL and 1^{st}-order VC

(c) FE-MUSCL and 3^{rd}-order VC

(d) FE-MUSCL and 5^{th}-order VC

Fig. 6. Error convergence for FE-MUSCL schemes with and without VC.

Table 4
Accuracy for the isentropic vortex case.

Scheme	Mesh	Baseline		With VC	
		$\log(L^2\ error)$	L^2 *order*	$\log(L^2\ error)$	L^2 *order*
FE-MUSCL1	25 × 25	1.0850		1.0774	
	50 × 50	0.9073	0.590	0.8933	0.612
	100 × 100	0.6697	0.789	0.6523	0.801
	200 × 200	0.4022	0.888	0.3836	0.893
	400 × 400	0.1186	0.942	0.0994	0.944
FE-MUSCL3	25 × 25	0.1740		0.0764	
	50 × 50	−0.7258	2.989	−0.8729	3.153
	100 × 100	−1.6046	2.919	−1.7063	2.769
	200 × 200	−2.4991	2.971	−2.6061	2.989
	400 × 400	−3.4001	2.993	−3.5051	2.986
FE-MUSCL5	25 × 25	−0.1413		0.1429	
	50 × 50	−1.3837	4.127	−1.1282	4.223
	100 × 100	−2.8237	4.783	−2.5886	4.852
	200 × 200	−4.3142	4.951	−4.2111	5.390
	400 × 400	−5.8159	4.989	−5.7172	5.003

isentropic vortex is initialized at $x_0 = y_0 = -10$ using the model of Yee et al. [37] as for the previous case. Time integration is performed with a classical 4-step explicit Runge–Kutta algorithm and a time step $\Delta t = 0.025$ for all cases, meaning an approximate $CFL \approx 0.083$. Note that a full advection is completed in time $T = 30$.

Space discretization is performed using 3rd- and 5th-order FE-MUSCL baseline schemes. The problem is solved on a coarse 100 × 100 and a medium 200 × 200 Cartesian grid with approximately 4 and 8 cells respectively across the vortex core radius and periodicity conditions are imposed at each side of the domain. It should be noted that the coarse 100^2 mesh case is not expected to display significant difference between VC schemes of different order. This is because the difference in the error convergence of high-order VC for such a coarse mesh ($\Delta x = 0.3$) is not significant with respect to the 1st-order one (see Figs. 6(a)–(d)). The purpose of this study is therefore to demonstrate the vorticity preserving capability of all orders of VC at very coarse meshes. In turn, the more refined 200^2 mesh is selected to demonstrate the increased com-

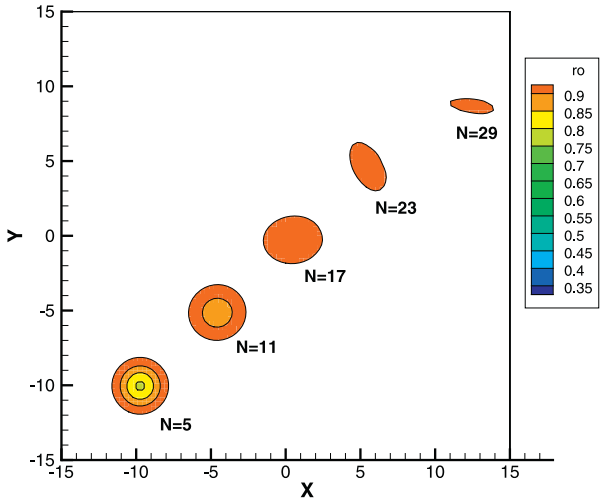

(a) Baseline FE-MUSCL3 scheme

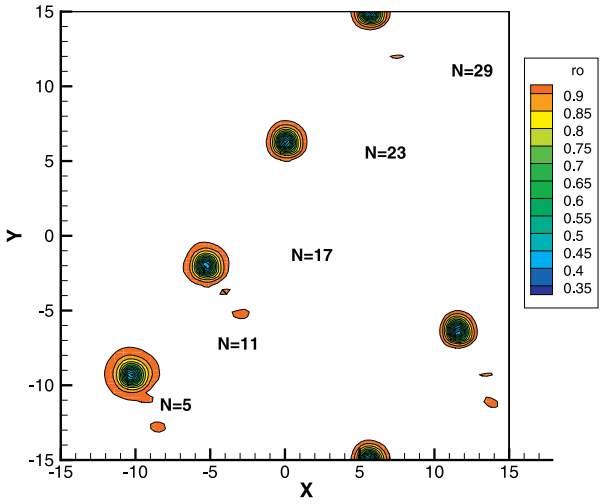

(b) FE-MUSCL3 and 1^{st}-order VC

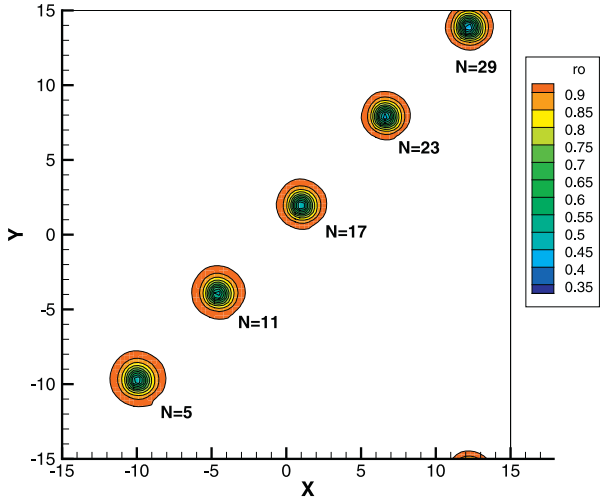

(c) FE-MUSCL3 and 3^{rd}-order VC

Fig. 7. Iso-density snapshots during the diagonal vortex advection. 3rd-order FE-MUSCL scheme on the 100^2 mesh. The approximate number of completed passages at each moment is indicated next to the corresponding contour.

patibility of high-order VC with high-order baseline flux discretizations. For the FE-MUSCL3 scheme we are solving the case on both meshes, whereas for the more precise FE-MUSCL5 we are only calculating the case on the coarse mesh. The advection is computed over a distance of 30 passages across the computational domain for the FE-MUSCL3 and 300 passages for FE-MUSCL5. For the cases where VC was applied, the value of the confinement parameters is defined empirically depending on the numerical error of the baseline scheme, corresponding to stronger VC for a case with important effect of dissipation, that is for a lower-order baseline scheme or a coarser mesh resolution. The coefficients used for the study are shown in Table 5.

Fig. 7 shows isodensity contours during the advection of the vortex for the FE-MUSCL3 case on the 100^2 mesh. The effect of dissipative error is severe for the baseline scheme leading to a complete diffusion of the vortex after 30 passages across the computational domain. The 1st-order VC method achieves a good preservation of vortex intensity, but introduces significant dispersion error along the vertical direction. The 3rd-order VC scheme has similar vorticity preserving capabilities with a more accurate trajectory prediction than the 1st-order one. Fig. 8 shows a more quantitative measure of preservation of vortex intensity through the evolution of minimum density, extracted at every passage across the computational domain. The effect of dissipation is apparent for the baseline scheme. For the more refined 200^2 mesh, the negative dissipation of the 1st-order VC term does not decrease according to the order of the baseline scheme, resulting in a rapid amplification of the advected structure as previously observed in [24]. For this reason, results on the fine mesh are presented for the 3rd-order VC only.

Table 5
Confinement parameters for the isentropic vortex advection.

Baseline scheme	Mesh	VC order	μ/ε	ε
FE-MUSCL3	100×100	1st	0.20	0.16
		3rd	0.20	0.16
	200×200	3rd	0.20	0.06
FE-MUSCL5	100×100	1st	0.40	0.02
		3rd	0.40	0.02
		5th	0.40	0.02

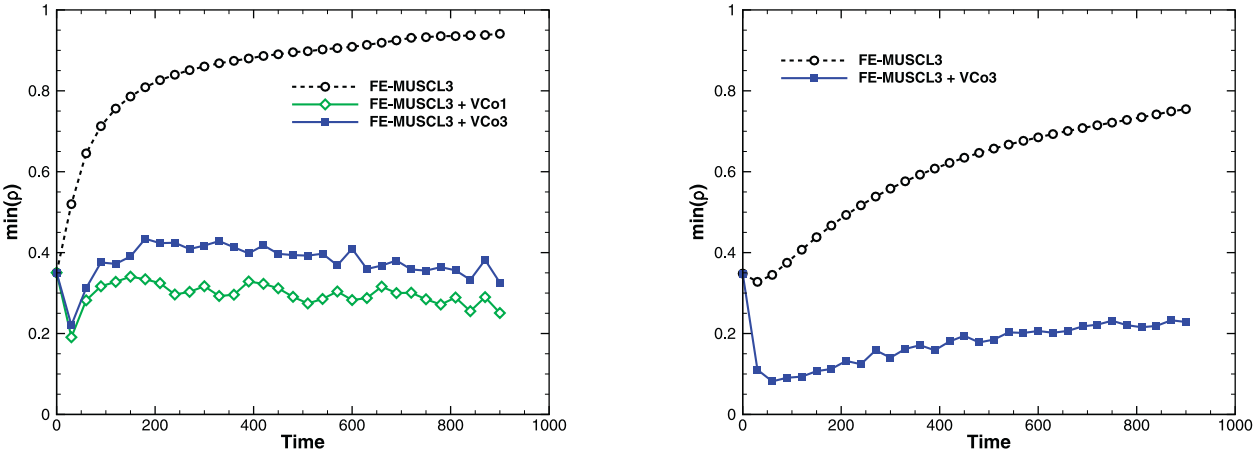

(a) 100^2 mesh (b) 200^2 mesh

Fig. 8. Time evolution of core density using FE-MUSCL3 and VC.

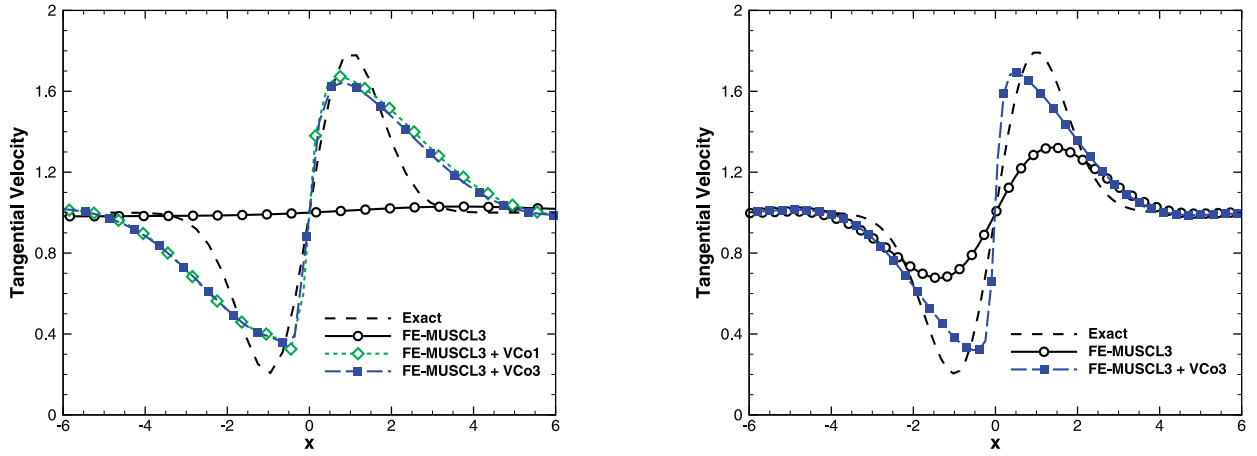

(a) 100^2 mesh (b) 200^2 mesh

Fig. 9. Comparison of tangential velocity profiles after 30 passages across the computational domain ($t = 900$) for the FE-MUSCL3 scheme with and without VC.

The evolution of core density also shows an initial amplification of the vortex intensity, which then quickly relaxes to a shape that satisfies the balance between the joint linear dissipation of the VC term and the baseline scheme against the negative nonlinear dissipation of the VC term. The initial stage of this mechanism might be related to the slightly positive values of the imaginary part of the modified wavenumber of confinement schemes already discussed in Section 3.2, since the spectral analysis portrays the characteristics of the numerical scheme for the calculation of a single time step and does not convey information on nonlinear mode interaction that occurs at later times. The vortex will eventually relax to an asymptotic shape that is advected without diffusion over arbitrarily long distances. However, this relaxation is significantly slower for VC of higher-order [22,24] and usually unreachable in realistic applications, meaning that results remain closer to the exact solution for VC of higher-order.

Horizontal extractions of tangential velocity profiles at the end of the computation are shown in Fig. 9 and are representative of the schemes' capability of preserving the shape of advected vortical structures. All curves have been centered at $x = 0$ for the sake of comparison. Computed profiles for schemes with and without VC show some spreading with respect to the exact solution, especially for the coarser mesh. However, VC clearly improves vorticity preservation for both meshes and produces satisfactory results especially in comparison to the baseline scheme and considering the length of the computed distance. The trajectory error with respect to the exact solution, which is the passive advection of the vortex along the diagonal, is shown in Fig. 10 as a measure of the schemes' phase approximation. Results are presented only for the coarser 100^2 mesh as trajectory errors are in the order of a few cells for the 200^2 case. The 1st-order VC exhibits an increased dispersion error in the vertical direction since the early stages of the advection. For 3rd-order VC, the difference with respect to the exact solution is equivalent to the baseline scheme.

There usually exist multiple pairs of confinement parameters $(\mu/\varepsilon, \varepsilon)$ that produce equivalent results in terms of vortex preservation, but it is not straightforward to identify whether the nonlinear dynamics of VC are similar depending on the absolute value of the parameters. On this basis, we are evaluating four different pairs of confinement parameters $(\mu/\varepsilon,\ \varepsilon) = \{(0.0, 0.10),\ (0.2, 0.16),\ (0.4, 0.40),\ (0.6, 1.80)\}$, for the FE-MUSCL3 and 3rd-order VC case on the coarser 100^2 mesh. These were obtained by prescribing μ/ε and identifying the value of ε which gives roughly equivalent preservation of the vortex. For such a case with significant effect of numerical dissipation (see Fig. 8(a)), a VC correction of relatively high magnitude is needed to preserve the vortex in the computation. Especially for high values of μ/ε, where numerical dissipation is further increased, the val-

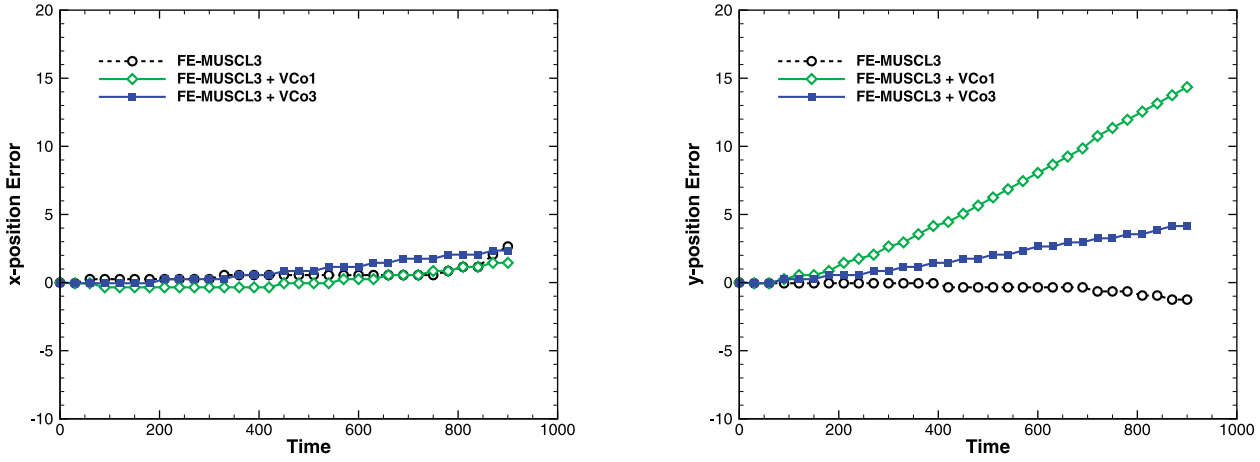

Fig. 10. Error in trajectory calculation for the FE-MUSCL3 scheme and VC on the 100^2 mesh.

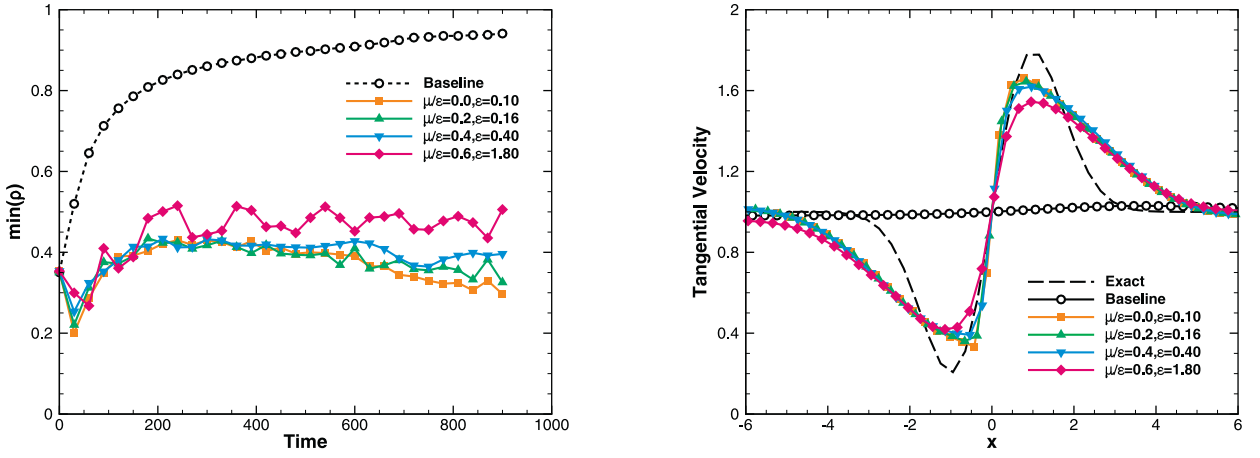

(a) Minimum density

(b) Velocity profiles at $t = 900$

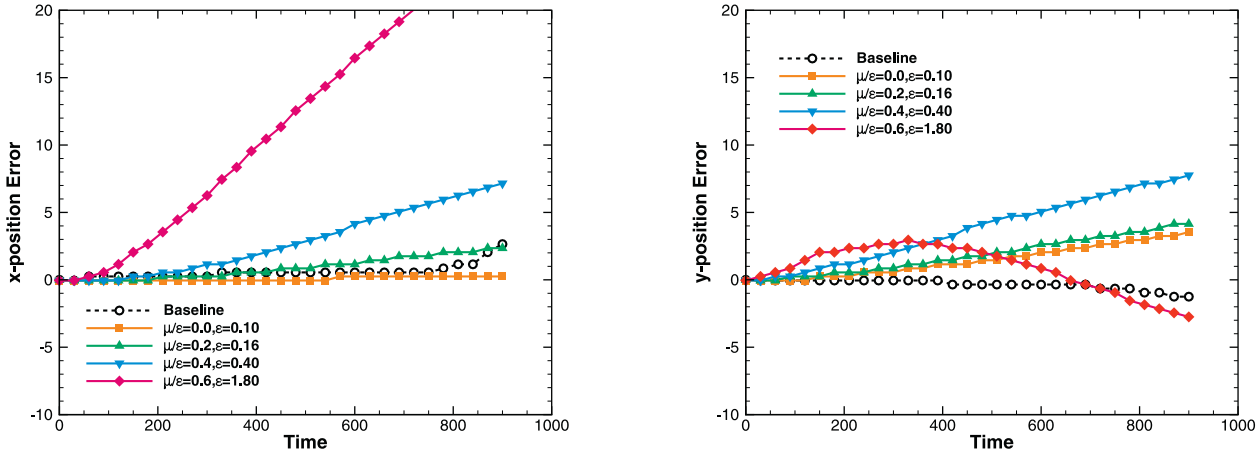

(c) x-position error

(d) y-position error

Fig. 11. Effect of different sets of confinement parameters $(\mu/\varepsilon, \varepsilon)$ for the FE-MUSCL3 and 3rd-order VC on the 100^2 mesh.

ues of ε needed to preserve the vortex are necessarily even larger than what is usually applied in computations, but differences in dynamics should be easier observed in such a scenario. Results of the comparison are presented in Fig. 11, showing that significantly higher values of the confinement parameters lead to a more irregular evolution of the vortex core density and to larger trajectory errors. The dispersion error however remains acceptable for reasonable values of ε, in the order of the scheme's artificial dissipation coefficient.

It is interesting to consider these results in analogy with the spectral analysis of Section 3.2, where it was demonstrated that the nonlinear negative dissipation of the VC term of Eq. (13) affects both the dispersive and dissipative properties of the discretization. For the Euler equations, that is in the absence of fluid viscosity, the

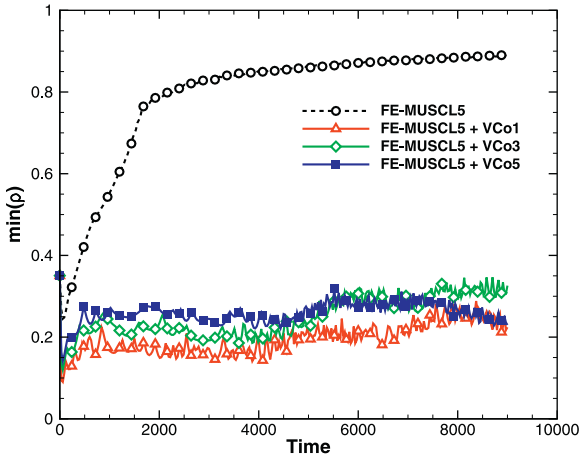

Fig. 12. Time evolution of core density using FE-MUSCL5 and VC on the 100^2 mesh.

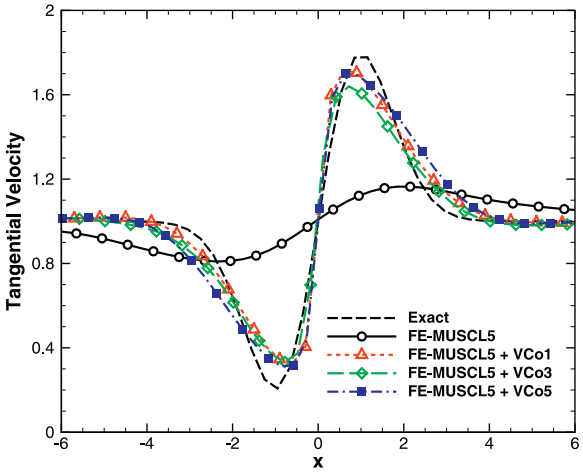

Fig. 13. Comparison of tangential velocity profiles after 300 passages across the computational domain ($t = 9000$) for the FE-MUSCL5 scheme with and without VC on the 100^2 mesh.

dissipation of the complete numerical scheme is defined from the balance between the linear artificial dissipation of Eqs. (27) and both the linear and nonlinear part of the VC term (13), meaning that an increased value of ε can easily be balanced by a reciprocally increased value of μ. However, the dispersion of the baseline scheme is defined from the convective flux approximation of Eqs. (27) and the dispersive effect of the nonlinear negative dissipation part of the VC term. In terms of confinement parameters, this means that the dissipation of the scheme is driven mainly by the balance between μ and ε, whereas dispersion is driven by ε.

Fig. 12 demonstrates that VC effectively balances the dissipation of the baseline scheme even at 5th-order of accuracy. Even though the effect of dissipation for the baseline scheme becomes important over time, the VC flux correction allows the overall steady preservation of the intensity of the vortex over the very long distance advection. More importantly, Fig. 13 shows that the profiles for the cases with VC show little spreading and are considerably closer to the exact solution than the baseline FE-MUSCL5. The trajectory error with respect to the exact solution is presented in Fig. 14. Again, the original 1st-order VC shows increased error in the vertical direction since early times. High-order VC schemes show overall decreased error compared to the baseline FE-MUSCL5, even though no clear conclusion can be made regarding the order of VC in this case.

It is clear in this study that schemes with VC have significantly improved vorticity preservation properties compared to baseline ones for all orders of the VC term. On very coarse meshes, high-order VC is not significantly closer to the exact solution compared to the original 1st-order one, the difference appearing mostly in terms of dispersion error. However, for finer meshes, the use of VC of the same order as the baseline scheme is important to guarantee consistency in terms of convergence towards the exact solution and to ensure that VC acts at a rate that matches the dissipation of the baseline scheme.

4.3. Viscous Taylor–Green Vortex

The final case is the study of the Taylor–Green Vortex (TGV) [38] at $Re = 1600$. The TGV flow is an unsteady problem solved in a periodic box $[2\pi]^3$ with an analytical two-dimensional initial condition for velocity that corresponds to large-scale vortices:

$$\begin{aligned} u(x,y,z,0) &= \sin x \cos y \cos z \\ v(x,y,z,0) &= -\cos x \sin y \cos z \\ w(x,y,z,0) &= 0 \end{aligned} \tag{45}$$

and an initial condition for pressure:

$$p(x,y,z,0) = p_0 + \frac{\rho}{16}(\cos(2x) + \cos(2y))(\cos(2z) + 2) \tag{46}$$

where $p_0 = 100$. The initial density field is considered constant $\rho\,(x,y,z,0) = \rho_0 = 1$. The fluid is considered a perfect gas with

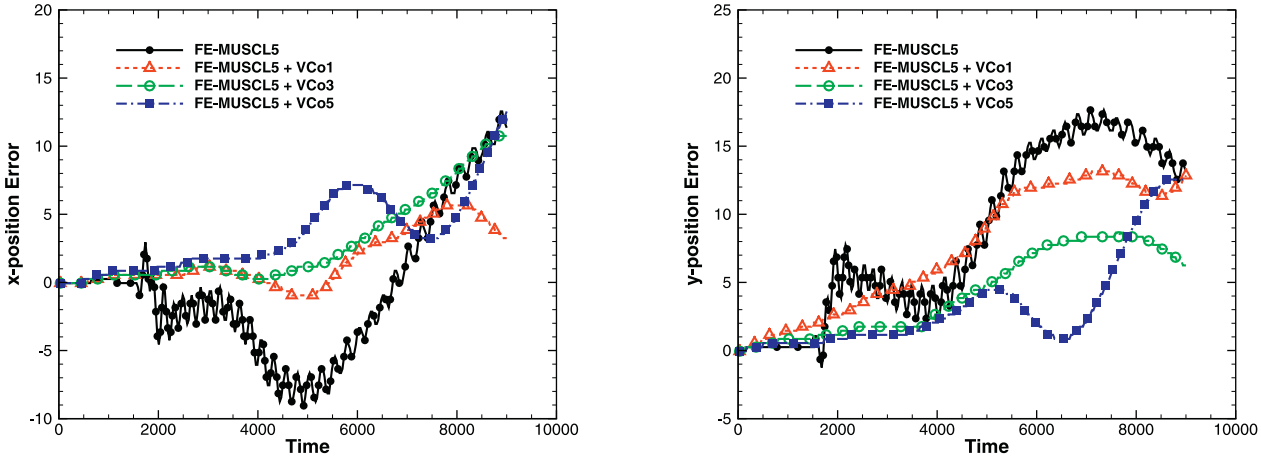

Fig. 14. Error in trajectory calculation for the FE-MUSCL5 scheme and VC on the 100^2 mesh.

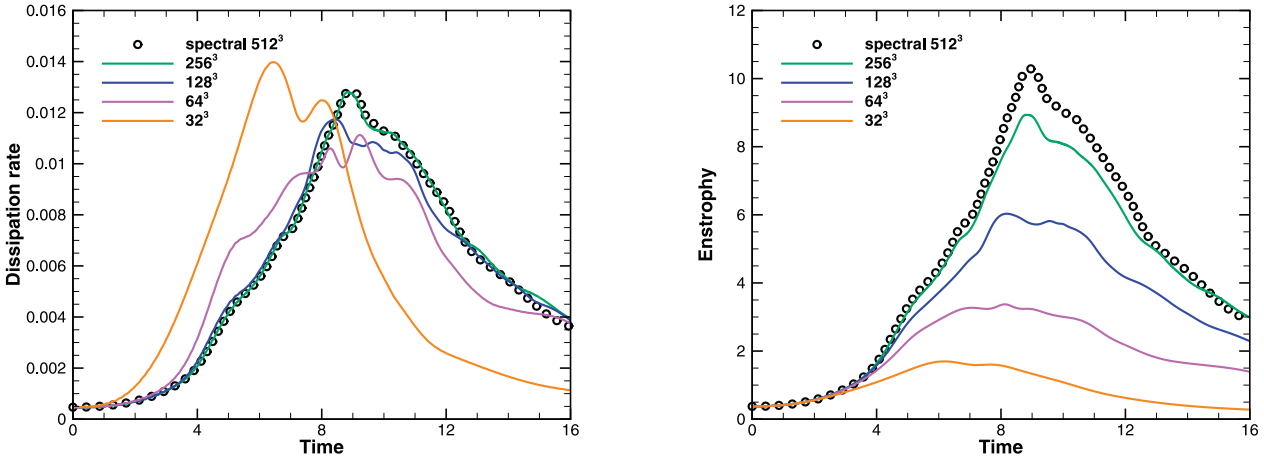

(a) Kinetic energy dissipation rate $-\frac{dK}{dt}$ (b) Enstrophy

Fig. 15. Grid convergence for the kinetic energy dissipation rate and the evolution of enstrophy using the baseline 5th-order FE-MUSCL scheme.

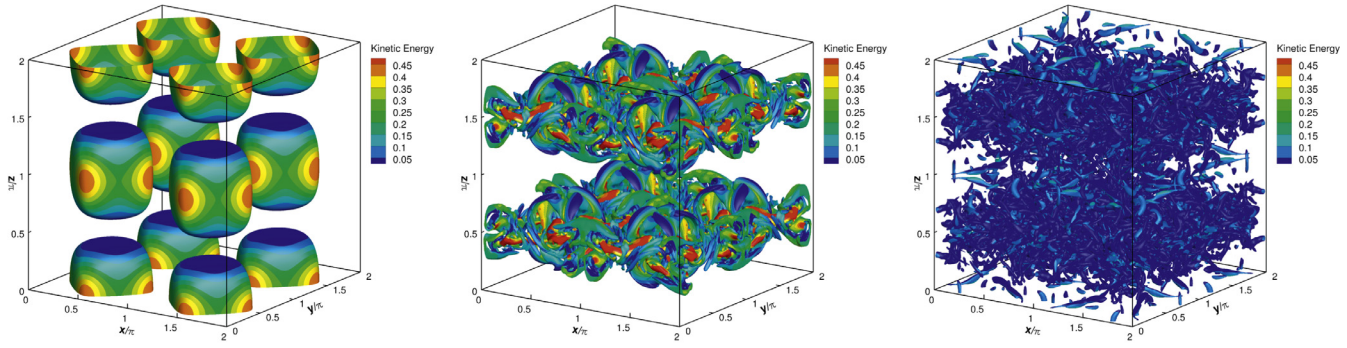

(a) $Q = 0.1$ at $t = 0$ (b) $Q = 2$ at $t = 8$ (c) $Q = 2$ at $t = 16$

Fig. 16. Iso-surfaces of the Q-criterion colored by kinetic energy computed with FE-MUSCL5 and 5th-order Vorticity Confinement on the 256^3 mesh.

zero bulk viscosity, $\gamma = 1.4$, and the Prandtl number is $Pr = 0.71$. Computations are performed for a low Mach number $M_0 = 0.10$ to allow comparison with reference simulations of the incompressible Navier–Stokes equations. All quantities have been adimensionalized with the reference velocity, density and length of the periodic box.

Despite the simplicity of the initial condition, the time evolution of the TGV flow consists of energy transfer from large to smaller scales through viscous, stretching and tilting mechanisms. For the viscous case, kinetic energy cascade occurs due to fluid viscosity and numerical dissipation as well as interaction and decay mechanisms that are characteristic of homogeneous turbulence. Due to the simplicity of the configuration and the complex represented phenomena, the TGV is a common benchmark case for high-order CFD workshops [21] and high-precision numerical methods [39–41].

It is therefore chosen as the last case to assess the robustness and performance of high-order Vorticity Confinement. The objective of this assessment is twofold. Having already proved the capability of VC to balance numerical dissipation in vortical flow regions and allow the advection of vortical structures over long distances, the primary objective is the investigation of the effect of VC in the dynamics of a complex and multi-scale flow, representative of a broad range of Large Eddy Simulation (LES) applications. The secondary objective is the evaluation of the improvement introduced by VC in the prediction of the TGV flow, compared to baseline upwind FE-MUSCL schemes.

The compressible Navier–Stokes equations are solved on Cartesian meshes of varying density with a total number of cells 32^3, 64^3, 128^3, 256^3. Convective fluxes are discretized using the 5th-order accurate FE-MUSCL scheme as for the previous studies, presented in Section 2.3. Time integration is performed using an explicit 6-stage Runge–Kutta algorithm, formally accurate to 2nd-order with coefficients that are optimized in the wavenumber space to ensure minimal dispersive and dissipative error [42]. The time step is set equal to 0.01/0.005/0.0025/0.00125 for the coarser to the finer mesh respectively, so that the *CFL* number is kept constant for all cases. For the cases with VC, the source term is always 5th-order accurate, as the baseline scheme. Two different sets of confinement parameters are presented, $\mu/\varepsilon = 0.4$, $\varepsilon = 0.02$ and $\mu/\varepsilon = 0.4$, $\varepsilon = 0.04$ where the first corresponds to standard values used in applications, such as for the diagonal vortex advection case of Section 4.2, and the second corresponds to doubling the magnitude of the VC term to test the robustness of the method. Results are compared against the reference of the International Workshop of High-Order CFD Methods, which is a converged DNS computation using a dealiased pseudo-spectral method on a 512^3 mesh. The resolution of the schemes is usually evaluated through the rate of dissipation of kinetic energy K. The integrated kinetic energy over the computational domain Ω is:

$$K = \frac{1}{\rho_0 \Omega} \int_\Omega \frac{1}{2} \rho ||\vec{u}||^2 \, d\Omega \tag{47}$$

The dissipation rate is computed directly from the kinetic energy as $-\frac{dK}{dt}$. Another similar measure is the time evolution of inte-

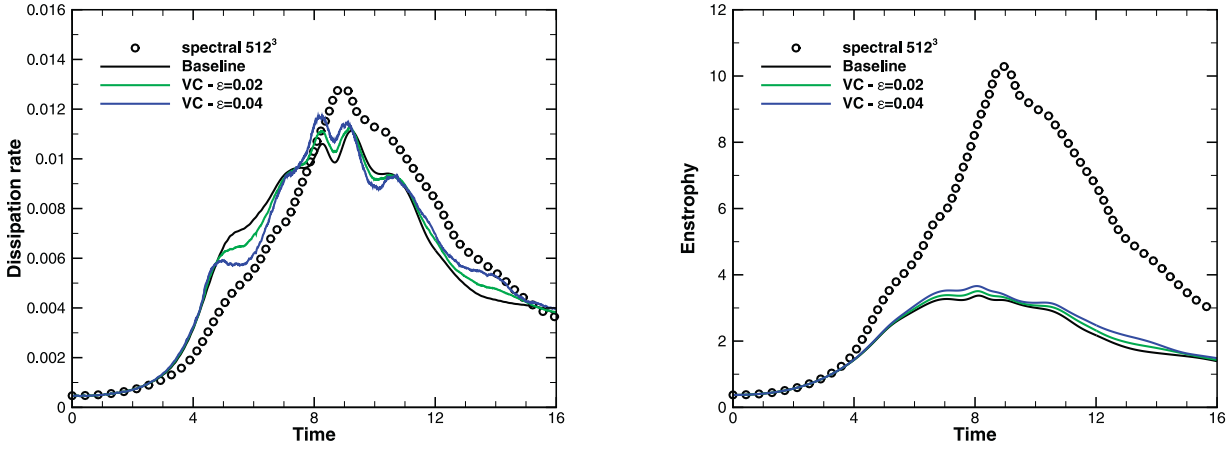

(a) 64^3 mesh

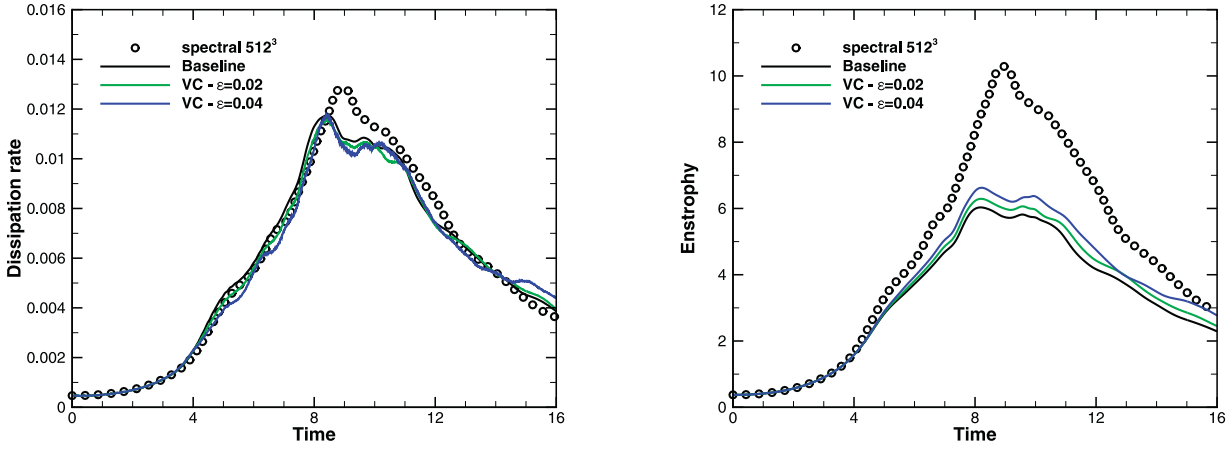

(b) 128^3 mesh

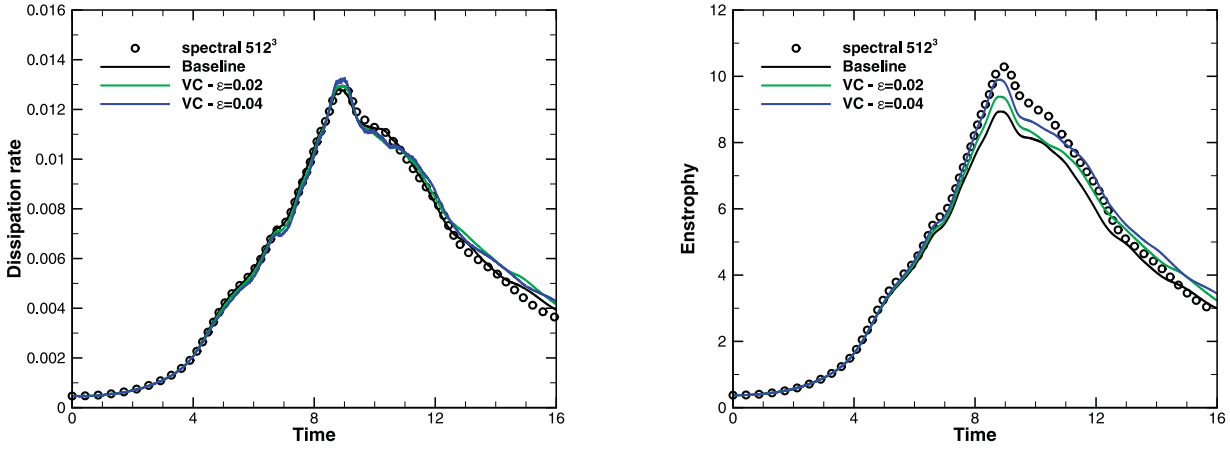

(c) 256^3 mesh

Fig. 17. Effect of VC on the kinetic energy dissipation rate $-\frac{dK}{dt}$ and the evolution of enstrophy for varying mesh density. FE-MUSCL5 and 5th-order Vorticity Confinement.

grated enstrophy over the computational domain:

$$\mathrm{E} = \frac{1}{\rho_0\,\Omega}\int_\Omega \frac{1}{2}\rho||\vec{\omega}||^2\,d\Omega \tag{48}$$

For an incompressible flow without numerical dissipation the kinetic energy dissipation rate is related to enstrophy via $-\frac{dK}{dt} = 2\frac{\mu}{\rho_0}E$. For the calculation of enstrophy through Eq. (48), velocity gradients are evaluated using the 7-point Dispersion-Relation-Preserving (DRP) scheme of Tam & Webb [43]. For the calculation of the VC term, velocity gradients are evaluated using a 2nd-order compact scheme equivalent to Gauss' divergence theorem to minimize the number of ghost cells required to accurately calculate the term on the domain boundaries (see Section 2.3).

Fig. 15 shows a grid convergence study for the baseline FE-MUSCL5 scheme. The dissipation rate converges fast towards the DNS results, that are well matched already on the 256^3 mesh, ex-

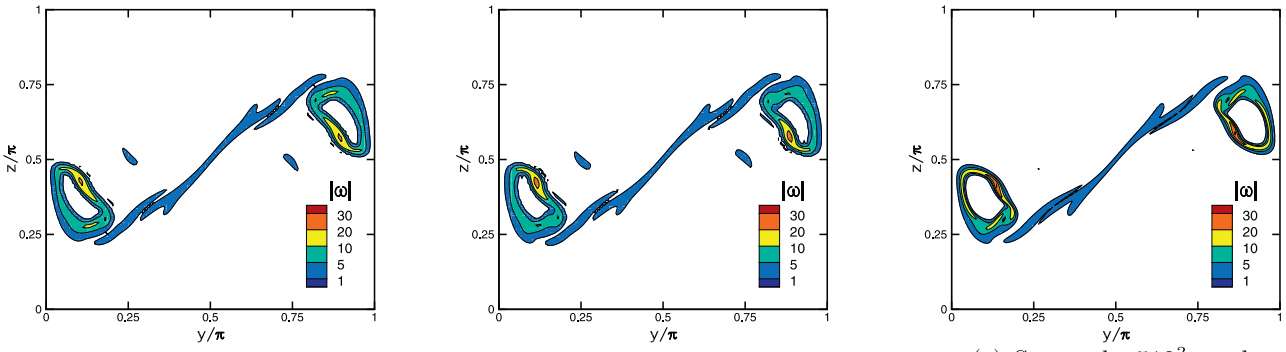

(a) Baseline FE-MUSCL5 - 256^3 mesh

(b) FE-MUSCL5 + VC - 256^3 mesh ($\varepsilon = 0.02$)

(c) Spectral - 512^3 mesh

Fig. 18. Iso-contours of the dimensionless vorticity norm $||\bar{\omega}||$ on the periodic face $x = 0$ at nondimensional time $t = 8$.

cept at later times during the end of the turbulence decay phase. The evolution of integrated enstrophy E over the domain is more difficult to match, since it contains the accumulated error in the computation of conservative variables and velocity gradients over the computational domain. It is thus often used as a criterion for the convergence of TGV flow calculations.

The TGV problem is initially dominated by vortex stretching and tilting mechanisms, generating smaller and smaller vortical structures up to the time at which the dissipation rate peaks ($t \approx 9$). The flow then transitions to fully developed non-isotropic turbulence and finally decays due to the dissipation acting at the smaller scales (snapshots of the flow computed with VC are shown in Fig. 16).

The left column of Fig. 17 shows the difference of the time evolution of the kinetic energy dissipation rate between the baseline case and the FE-MUSCL5 scheme with VC. On the 64^3 and 256^3 meshes, the dynamics of the scheme with VC are consistent with the vorticity dynamics of the flow, reducing dissipation during the vortex stretching phase and later on increasing the dissipation peak since it improves the preservation of small structures that largely contribute to this dissipation. For the 128^3 case however, VC is constantly reducing dissipation but does not increase the dissipation peak. Results also show that a large increase of the confinement parameter ε, or equivalently a large increase of the magnitude of the VC flux correction, leads to sharper changes of the dissipation rate during the flow evolution. Out of the two sets of parameters, the case $\varepsilon = 0.02$ gives results that are closer to the reference solution, especially for the 128^3 mesh during the vortex stretching phase.

Furthermore, the effect of VC is smaller when the mesh is refined, or equivalently when numerical dissipation is reduced, displaying consistent behavior with the baseline 5th-order FE-MUSCL scheme for the vortex stretching phase and up to the development of turbulence. Regarding this last stage, VC increases the resolved dissipation compared to the baseline scheme due to the improved preservation of eddies in the inertial range, even when the baseline case is quite well-converged towards the reference results. This behavior is however also observed for the baseline FE-MUSCL5 scheme (Fig. 15(a)).

The time evolution of enstrophy is shown in the right column of Fig. 17 for the same cases. Results are straightforward meaning that VC acts in vortical regions by introducing negative dissipation in the vorticity transport equation and therefore increases the integral value of enstrophy, in a sense accelerating the convergence towards the DNS solution. Contrary to the decrease of the effect of VC on the kinetic energy dissipation rate with mesh refinement, its influence is more important on the calculation of enstrophy. Since the magnitude of the VC term decreases with mesh refinement according to the order of accuracy, similarly to the baseline scheme's artificial dissipation, this indicates that the efficiency of VC on the finer meshes is related to the better alignment of the term with local vorticity.

The consistency of high-order VC extensions is further demonstrated by the isocontours of the dimensionless vorticity norm on a periodic face of the computational domain at $t = 8$, presented in Fig. 18. Results of the VC and baseline FE-MUSCL5 scheme are compared to the reference spectral computation and provide a good approximation of the main flow structures. The case with VC shows improved preservation of vortices compared to the baseline scheme, without any introduction of spurious structures.

It can be argued that the efficiency of VC and its high-order extensions is dependent on the precision of the vorticity field, or equivalently the velocity gradient calculation scheme, since the VC flux correction is calculated based on vorticity (see Section 2.2). To assess this dependence, different velocity gradient calculation schemes are compared for the 128^3 mesh using the FE-MUSCL5 with VC and confinement parameters $\mu/\varepsilon = 0.4$, $\varepsilon = 0.02$. The evaluated schemes are the standard 2nd-order compact scheme which is equivalent to Gauss' divergence theorem and used for the previous results, two large-stencil standard schemes which achieve the maximum order of accuracy on the given stencil and the formally 4th-order accurate 13-point DRP scheme of Bogey & Bailly with optimized coefficients in the wavenumber space [42]. The two standard schemes are 5th- and 9th-order accurate on a 7- and 11-point stencil respectively. All aforementioned orders of accuracy refer to Cartesian grids. A comparison of the results is presented in Fig. 19. The evolution of the kinetic energy dissipation rate shows that the scheme's influence is small up to time $t = 9$ where dissipation peaks and vortical structures are well resolved by all schemes. The 13-point DRP and the optimal order standard schemes produce very similar results for the complete time evolution of the flow. The Gauss scheme is in very good agreement with high-resolution schemes up to the dissipation peak. It does however display a difference with respect to high-accuracy schemes during the turbulence decay phase, since quality of the solution is largely-dependent on the resolution of small structures. The calculated enstrophy is similar for all schemes, with a smaller difference between Gauss and high-precision schemes at the turbulence decay phase than for the kinetic energy dissipation rate.

This study shows that schemes with VC are consistent with the dynamics of the complex TGV flow without the need for a special treatment or a more sophisticated choice of confinement parameters compared to standard applications. Furthermore, the developed VC schemes introduce an improvement to the baseline

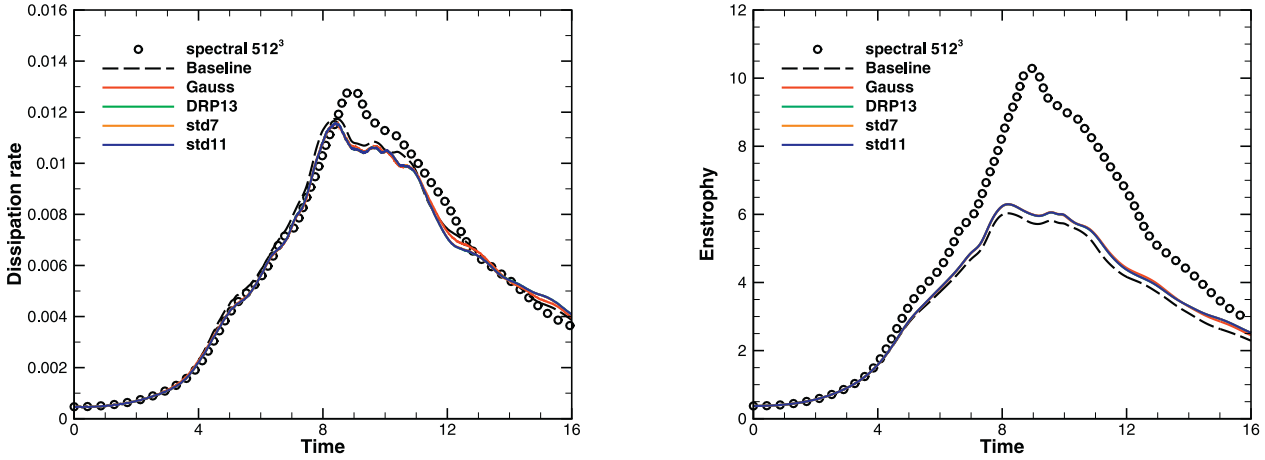

(a) Kinetic energy dissipation rate $-\frac{dK}{dt}$ (b) Enstrophy

Fig. 19. Influence of the velocity gradient calculation scheme. FE-MUSCL5 and 5th-order Vorticity Confinement, $\mu/\varepsilon = 0.4$, $\varepsilon = 0.02$, 128^3 mesh.

scheme over the vortex stretching phase where the treatment of large structures is involved. However, VC increases the life-span of vortices during the turbulence decay phase, eventually producing more dissipation at the smallest scales, a behavior which might be related to the properties of the baseline flux discretization but should be improved in the future.

5. Conclusions

This work presents extensions of Vorticity Confinement up to 5th-order of accuracy for the calculation of compressible vortical flows. For the scalar transport case, the high-order confinement formulation is presented for decoupled schemes in space and time. A linear analysis is inadequate for VC schemes, since it shows that they are unstable, contrary to extensive numerical results. A numerical quasi-linear analysis allows to prove that space discretizations with confinement are numerically stable and have both improved dispersive and dissipative properties compared to their linear counterparts. This effect remains at higher orders since confinement is based on a high-order dissipation operator and therefore introduces nonlinear negative dissipation accordingly to the dissipative error of the baseline scheme. Last, the eigenvalues of these schemes lie within the stability region of classical 3-step and 4-step Runge–Kutta algorithms and show small sensitivity to the choice of the confinement parameter.

For the Euler and Navier–Stokes equations, the original VC method is extended up to 5th-order of accuracy for Cartesian meshes using the methodology developed in [24]. The formulation remains conservative, independent of the choice of baseline numerical scheme and rotationally invariant since it is based on the Laplace operator. Furthermore, both the original VC method and its high-order extensions are shown to be equivalent to a nonlinear anti-diffusive flux correction explicitly based on vorticity.

The actual order of accuracy of the high-order VC extensions is first evaluated in the case of a static isentropic vortex. The schemes are then applied to the case of a long distance diagonal vortex advection. In this inviscid case, schemes with VC provide results considerably closer to the exact solution than the baseline scheme, allowing the calculation of the advection of vortices over very long distances with small dissipation. Furthermore, schemes with high-order VC are shown to be more accurate in terms of vortex trajectory prediction than the original VC. Numerical experiments indicate that there exists a wide range of pairs of confinement parameters yielding similar vorticity preservation, but too large values of these parameters tend to introduce additional dispersive errors in the calculation. In practice however, dispersion errors were found to be low for values of confinement parameters in the order of magnitude of the baseline artificial dissipation coefficient. Additional results for the viscous Taylor–Green Vortex case demonstrate the robustness of high-order VC schemes and their consistency with complex vorticity dynamics, whereas high-order VC is also shown to improve the calculation of enstrophy, even at fine meshes. Finally, the efficiency of high-order VC is shown to have small dependence on the velocity gradient calculation scheme, with differences between low- and high-precision methods appearing in the treatment of smaller scales.

High-order Vorticity Confinement consistently balances the excess dissipation of the scheme in vortical regions and improves the calculation of vorticity in numerical simulations for both simple advection cases and more complex dynamics. Due to its nonlinear formulation, it is also demonstrated to have an additional effect on the dispersive properties of the numerical scheme, but this effect has been found to be small for the cases investigated in this article, and even beneficial for reasonable values of the confinement parameters. Overall, high-order VC is an interesting approach for high-order simulations of vortical flows, combining the vorticity-preserving properties of the original 1st-order VC and preserving the accuracy order of the baseline method.

Acknowledgments

The authors would like to thank Cedric Content from the DynFluid Laboratory and Bertrand Michel from the Computational Fluid Mechanics department of ONERA for discussions on the numerical implementation of the method. This research was co-funded by ONERA and a DGA-MRIS scholarship under the convention 2014-60-0055.

References

[1] Leishman J, Bhagwat M, Bagai A. Free-vortex filament methods for the analysis of helicopter rotor wakes. J Aircr 2002;39(5):759–75.
[2] Winckelmans G, Cocle R, Dufresne L, Capart R. Vortex methods and their application to trailing wake vortex simulations. C R Phys 2005;6(4–5):467–86. http://dx.doi.org/10.1016/j.crhy.2005.05.001. Aircraft trailing vortices; http://www.sciencedirect.com/science/article/pii/S1631070505000575.
[3] Cottet G-H, Koumoutsakos PD. Vortex methods: theory and practice. Cambridge University Press; 2000.
[4] Joubarne E, Guibault F, Braun O, Avellan F. Numerical capture of wing tip vortex improved by mesh adaptation. Int J Numer Methods Fluids 2011;67(1):8–32.

[5] Fidkowski K, Roe P. An entropy adjoint approach to mesh refinement. SIAM J Sci Comput 2010;32(3):1261–87.
[6] Kamkar S, Wissink AM, Sankaran V, Jameson A. Feature-driven cartesian adaptive mesh refinement for vortex-dominated flows. J Comput Phys 2011;230(16):6271–98.
[7] de la Llave Plata M, Couaillier V, Marmignon C, Le Pape M-C, Gazaix M, Cantaloube B. Further developments in the multiblock hybrid CFD solver elsA-H. 50th AIAA aerospace sciences meeting, AIAA paper 2012-1112; 2012.
[8] Sankaran V, Wissink A, Datta A, Sitaraman J, Potsdam M, Jayaraman B, et al. Overview of the Helios version 2.0 computational platform for rotorcraft simulations Aerospace sciences meetings. American Institute of Aeronautics and Astronautics; 2011. doi:10.2514/6.2011-1105.
[9] Papadakis G, Voutsinas SG. In view of accelerating CFD simulations through coupling with vortex particle approximations. In: Journal of Physics: Conference Series, 524. IOP Publishing; 2014. p. 012126.
[10] Oxley GS. A 2-D hybrid Euler-compressible vortex particle method for transonic rotorcraft flows. Carleton University Ottawa; 2009.
[11] Balsara DS, Garain S, Shu C-W. An efficient class of WENO schemes with adaptive order. J Comput Phys 2016;326:780–804.
[12] Kroll N, Hirsch C, Bassi F, Johnston C, Hillewaert K. IDIHOM: industrialization of high-order methods-a top-down approach: results of a collaborative research project funded by the European Union, 2010–2014, 128. Springer; 2015.
[13] Asthana K, Jameson A. High-order flux reconstruction schemes with minimal dispersion and dissipation. J Sci Comput 2015;62(3):913–44.
[14] Morton K, Roe PL. Vorticity-preserving Lax–Wendroff-type schemes for the system wave equation. SIAM J Sci Comput 2001;23(1):170–92.
[15] Lerat A, Falissard F, Sidès J. Vorticity-preserving schemes for the compressible Euler equations. J Comput Phys 2007;225(1):635–51. http://dx.doi.org/10.1016/j.jcp.2006.12.025. http://www.sciencedirect.com/science/article/pii/S0021999106006140.
[16] Steinhoff J, Lynn N. Treatment of vortical flow using vorticity confinement. In: Frontiers of computational fluid dynamics. World Scientific; 2006. p. 199–237. doi:10.1142/9789812703187_0010.
[17] Steinhoff J, Lynn N, Wang L. Large eddy simulation using vorticity confinement. Implicit large Eddy simulations: computing turbulent flow dynamics. Cambridge University Press; 2006a.
[18] Steinhoff J, Lynn N, Yonghu W, Fan M, Wang L, Dietz W. Turbulent flow simulations using vorticity confinement. Implicit large Eddy simulations: computing turbulent flow dynamics. Cambridge University Press; 2006b.
[19] Steinhoff J, Puskas E, Babu S, Wenren Y, Underhill D. Computation of thin features over long distances using solitary waves. In: AIAA paper 97–1976, 13th computational fluid dynamics conference.Snowmass, Colorado; 1997.
[20] Steinhoff J, Dietz W, Haas S, Xiao M, Lynn N, Fan M. Simulating small scale features in fluid dynamics and acoustics as nonlinear solitary waves. AIAA paper 2003-078, 41st Aerospace meeting and exhibit. Reno, Nevada; 2003.
[21] Wang ZJ, Fidkowski K, Abgrall R, Bassi F, Caraeni D, Cary A, et al. High-order CFD methods: current status and perspective. Int J Numer Methods Fluids 2013;72(8):811–45. doi:10.1002/fld.3767.
[22] Costes M, Juillet F. Analysis and higher-order extension of the VC2 confinement scheme. Comput Fluids 2012;56(0):102–17. http://dx.doi.org/10.1016/j.compfluid.2011.12.002. http://www.sciencedirect.com/science/article/pii/S0045793011003653.
[23] Costes M. Development of a 3rd-order vorticity confinement scheme for rotor wakes simulations. 38th European Rotorcraft Forum. Amsterdam, The Netherlands; 2012.
[24] Costes M, Petropoulos I, Cinnella P. Development of a third-order accurate vorticity confinement scheme. Comput Fluids 2016;136:132–51. http://dx.doi.org/10.1016/j.compfluid.2016.05.025. http://www.sciencedirect.com/science/article/pii/S0045793016301736.
[25] Lerat A, Corre C. High-order residual-based compact schemes on structured grids. CFD-Higher order discretization methods. VKI-LS 2006-01. von Karman Institute for Fluid Dynamics; 2006.
[26] Hirsch C. Numerical computation of internal and external flows: the fundamentals of computational fluid dynamics: the fundamentals of computational fluid dynamics. Butterworth-Heinemann; 2007.
[27] Costes M. Analysis of the second vorticity confinement scheme. Aerosp Sci Technol 2008;12(3):203–13. http://dx.doi.org/10.1016/j.ast.2007.06.004. http://www.sciencedirect.com/science/article/pii/S1270963807000831.
[28] Després B, Lagoutière F. Contact discontinuity capturing schemes for linear advection and compressible gas dynamics. J Sci Comput 2001;16(4):479–524.
[29] Xu Z, Shu C-W. Anti-diffusive flux corrections for high order finite difference WENO schemes. J Comput Phys 2005;205(2):458–85.
[30] Outtier P-Y, Content C, Cinnella P, Michel B. The high-order dynamic computational laboratory for CFD research and applications. Fluid dynamics and co-located conferences. American Institute of Aeronautics and Astronautics; 2013. doi:10.2514/6.2013-2439.
[31] Haller G. An objective definition of a vortex. J Fluid Mech 2005;525:1–26.
[32] Vichnevetsky R, Bowles J. Fourier analysis of numerical approximations of hyperbolic equations. Soc Ind Appl Math; 1982. doi:10.1137/1.9781611970876.
[33] Costes M. Stability analysis of the VC2 confinement scheme for the linear transport equation. Comput Fluids 2013;86(0):537–57. http://dx.doi.org/10.1016/j.compfluid.2013.07.026. http://www.sciencedirect.com/science/article/pii/S0045793013003058.
[34] Pirozzoli S. On the spectral properties of shock-capturing schemes. J Comput Phys 2006;219(2):489–97. http://dx.doi.org/10.1016/j.jcp.2006.07.009. http://www.sciencedirect.com/science/article/pii/S0021999106003482.
[35] Cunha G, Redonnet S. On the effective accuracy of spectral-like optimized finite-difference schemes for computational aeroacoustics. J Comput Phys 2014;263:222–32.
[36] Grimich K, Cinnella P, Lerat A. Spectral properties of high-order residual-based compact schemes for unsteady compressible flows. J Comput Phys 2013;252:142–62.
[37] Yee H, Vinokur M, Djomehri M. Entropy splitting and numerical dissipation. J Comput Phys 2000;162(1):33–81. http://dx.doi.org/10.1006/jcph.2000.6517. http://www.sciencedirect.com/science/article/pii/S0021999100965173.
[38] Taylor GI, Green AE. Mechanism of the production of small eddies from large ones. Proc R Soc London A 1937;158(895):499–521. doi:10.1098/rspa.1937.0036.
[39] Bull JR, Jameson A. Simulation of the Taylor–Green vortex using high-order flux reconstruction schemes. AIAA J 2015;53(9):2750–61.
[40] Van Rees WM, Leonard A, Pullin D, Koumoutsakos P. A comparison of vortex and pseudo-spectral methods for the simulation of periodic vortical flows at high reynolds numbers. J Comput Phys 2011;230(8):2794–805.
[41] Lerat A. An efficient high-order compact scheme for the unsteady compressible Euler and Navier–Stokes equations. J Comput Phys 2016;322:365–86.
[42] Bogey C, Bailly C. A family of low dispersive and low dissipative explicit schemes for flow and noise computations. J Comput Phys 2004;194(1):194–214.
[43] Tam CKW, Webb JC. Dispersion-relation-preserving finite difference schemes for computational acoustics. J Comput Phys 1993;107(2):262–81.